



# Causes of the long-term variability of southwestern South America precipitation in the IPSL-CM6A-LR model

Julián Villamayor<sup>1</sup> · Myriam Khodri<sup>1</sup> · Ricardo Villalba<sup>2</sup> · Valérie Daux<sup>3</sup>

Received: 22 September 2020 / Accepted: 6 May 2021 / Published online: 15 May 2021  
© The Author(s), under exclusive licence to Springer-Verlag GmbH Germany, part of Springer Nature 2021

## Abstract

Southwestern South America (SWSA) has undergone frequent and persistent droughts in recent decades with severe impacts on water resources, and consequently, on socio-economic activities at a sub-continental scale. The local drying trend in this region has been associated with the expansion of the subtropical drylands over the last decades. It has been shown that SWSA precipitation is linked to large-scale dynamics modulated by internal climate variability and external forcing. This work aims at unravelling the causes of this long-term trend toward dryness in the context of the emerging climate change relying on a large set simulations of the state-of-the-art IPSL-CM6A-LR climate model from the 6th phase of the Coupled Model Intercomparison Project. Our results identify the leading role of dynamical changes induced by external forcings, over the local thermodynamical effects and teleconnections with internal global modes of sea surface temperature. Our findings show that the simulated long-term changes of SWSA precipitation are dominated by externally forced anomalous expansion of the Southern Hemisphere Hadley Cell (HC) and a persistent positive Southern Annular Mode (SAM) trend since the late 1970s. Long-term changes in the HC extent and the SAM show strong co-linearity. They are attributable to stratospheric ozone depletion in austral spring-summer and increased atmospheric greenhouse gases all year round. Future ssp585 and ssp126 scenarios project a dominant role of anthropogenic forcings on the HC expansion and the subsequent SWSA drying, exceeding the threshold of extreme drought due to internal variability as soon as the 2040s, and suggest that these effects will persist until the end of the twenty-first century.

**Keywords** Subtropical Andes drying trend · Hadley Cell expansion · Decadal variability · External forcing · CMIP6 · Detection and attribution · Future scenarios

## 1 Introduction

The southwestern South America (SWSA) region encompasses the Andean Cordillera and adjacent territories from the Pacific coast to the continental arid lowlands in Argentina and south of the dry Altiplano. This region is characterized by a marked precipitation gradient from <100 mm in the north (25–28°S) to well over 2000 mm in the south

(40–45°S). Precipitation primarily occurs during austral winter (June–August, JJA) associated with passing fronts embedded in the mid-latitude Westerly flow and enhanced by the orographic effect of the Andes Mountains (Montecinos and Aceituno 2003; Garreaud et al. 2013; Viale et al. 2019). Latitudinal variations in the southeastern Pacific anticyclone and the subtropical jet stream modulate the seasonality of these fronts, which commonly form at the poleward limit of the Southern Hemisphere (SH) Hadley Cell (HC) (Montecinos and Aceituno 2003; Barrett and Hameed 2017). Closely linked to large-scale atmospheric circulation, SWSA precipitation supports the many glaciers and lakes in the Andes and contributes to the flow of major streams and rivers along the Cordillera. Indeed, most rivers originate in the upper Andes, where precipitation is comparatively higher than in adjacent territories (Masiokas et al. 2019). With some regional differences, SWSA has undergone a striking drying trend since the 1980s (e.g., Garreaud et al. 2013,

✉ Julián Villamayor  
julian.villamayor@locean.ipsl.fr

<sup>1</sup> LOCEAN-IPSL, Sorbonne Université/CNRS/IRD/MNHN, 4 place Jussieu, 75005 Paris, France

<sup>2</sup> Instituto Argentino de Nivología, Glaciología y Ciencias Ambientales (CCT-Mendoza/CONICET), Mendoza, Argentina

<sup>3</sup> Laboratoire des Sciences du Climat et de l'Environnement (LSCE, CEA/CNRS/UVSQ), Gif-sur-Yvette, France

2017, 2020; Boisier et al. 2016, 2018), with marked glacier retreats and lake-area reductions without precedent over the last millennium (Garreaud et al. 2017; Pabón-Cañedo et al. 2020). A robust drying trend of around  $-28$  mm per decade during the austral winter rainy season has been found in the southern part of SWSA (Boisier et al. 2018). In the northern drier regions, the larger amplitude of the high-frequency variability in austral summer (December–February, DJF) and fall (March–May, MAM) complicates the detection of consistent trends in precipitation. However, a reduction in river streamflows suggests that a drying tendency is also taking place in spring (September–October, SON) and summer in the north sector of SWSA (Boisier et al. 2018). Although they display lower drought than observed, model simulations for the historical period of the 5th phase of the Coupled Model Intercomparison Project (CMIP5) can capture such drying tendency in response to external anthropogenic forcings (Vera and Díaz 2015; Boisier et al. 2018). Due to the important socio-economic and ecological impacts of changes in water resources in SWSA (CR2 2015; Norero and Bonilla 1999; Rosegrant et al. 2000; Meza et al. 2012), it is critical to investigate further and quantify the potential impacts of climate change in this region.

Low-frequency rainfall changes in SWSA are also associated with internal climate variability. Indeed, during austral winter and spring, SWSA annual moisture conditions are tightly linked to the southeastern Pacific sea surface temperature (SST) variability (Rutllant and Fuenzalida 1991; Garreaud et al. 2009; Quintana and Aceituno 2012; Boisier et al. 2016) related to the El Niño Southern Oscillation (ENSO), the leading mode of interannual climate variability in the Pacific Ocean (e.g., McPhaden et al. 2006). Long-term ENSO fluctuations imprint a pan-Pacific pattern of coherent SST decadal variability (Newman et al. 2016) through atmospheric teleconnections (e.g., Alexander et al. 2002). This pattern is known as the Interdecadal Pacific Oscillation (IPO) and is the leading mode of internal, decadal to multidecadal variability in the Pacific Ocean (Folland et al. 1999; Meehl and Hu 2006). It is also typically referred to as its manifestation in the wintertime North Pacific SST, the so-called Pacific Decadal Oscillation (Mantua et al. 1997). During the positive (negative) phase, the IPO is characterized by an ENSO-like pattern of warm (cold) SST anomalies across the tropical Pacific, which extends in the subtropics over the eastern boundaries of the Pacific Ocean (Trenberth and Hurrell 1994; Meehl et al. 2009). The IPO has experienced a trend from a positive (i.e., El Niño-like) to a negative (La Niña-like) phase over the 1980–2014 period associated with an anomalous southward shift and spin-up of the southeastern Pacific anticyclone (Jebri et al. 2020) and of the mid-latitude storm-tracks over SWSA during the rainy season (Quintana and Aceituno 2012; Boisier et al. 2016, 2018). Thus, the concurrent IPO shift from positive to negative

phase might have contributed to the current prevailing SWSA dry conditions (Masiokas et al. 2010; Quintana and Aceituno 2012; Boisier et al. 2016). However, during DJF and MAM seasons, rainfall interannual-to-decadal fluctuations are also significantly influenced by the dominant mode of atmospheric circulation variability in the mid-latitudes of the SH, the Southern Annual Mode (SAM), also known as the Antarctic Oscillation (Gong and Wang 1999; Thompson and Wallace 2000; Thompson et al. 2000). During SAM positive phases, a zonally symmetric atmospheric pressure gradient is observed with negative and positive anomalies over Antarctica and the mid-latitudes, respectively, favoring an anomalous poleward shift of the circumpolar westerlies and more constrained zonal flow in mid-latitudes (Thompson and Wallace 2000; Thompson et al. 2000), resulting in less frontal rainfall in SWSA (Garreaud et al. 2009). These symmetric features and the impact on SWSA precipitation are reversed during the negative SAM phase.

The SWSA drying trends over recent decades could also result from external forcings. For instance, an intensification of the global hydrological cycle is projected under global warming due to a more extensive water vapour loading of the atmosphere, resulting in enhanced E–P (evaporation minus precipitation) in evaporative regions, and reduced E–P in precipitative regions according to the “wet-get-wetter, dry-get-drier” paradigm (Held and Soden 2006; Seager et al. 2010). Several observational datasets, CMIP5 models and reanalyses also suggest an essential role of externally forced large-scale dynamical changes. Observed southward shifts of the subtropical drying regions and mid-latitudes baroclinic eddies during late austral spring and summer have been associated with the SAM positive trend and the expansion of the HC in recent decades (e.g., Gillett and Thompson 2003; Previdi and Liepert 2007; Quintana and Aceituno 2012; Boisier et al. 2018). The HC expansion and SAM positive trends have both been attributed to increasing atmospheric greenhouse gases (GHGs) concentration and stratospheric ozone depletion (e.g., Polvani et al. 2011; Kim et al. 2017; Jebri et al. 2020). However, the tendency toward more La Niña events in relation to the recent IPO trend may also contribute to the HC poleward shift (Nguyen et al. 2013; Allen and Kovilakam 2017) and to more frequent positive SAM phases (Carvalho et al. 2005; Fogt et al. 2012). The counteracting effect of the recent ozone recovery (Eyring et al. 2010) and the intensification of GHGs effect (Andreae et al. 2005) is a source of uncertainty for the understanding of the future state of these modes (Fogt and Marshall 2020).

To our knowledge, previous studies have not explicitly examined (i) the respective contribution of anthropogenic forcing and internal climate variability on the decadal-to-longer term variance of SWSA rainfall throughout the last century and a half and (ii) the specific role of direct thermodynamical and dynamical changes in SWSA related to the

HC expansion and SAM trend. These are two major points that are addressed in this study along with (iii) the attribution of the modulation of SWSA precipitation to specific sources of external forcing over the last decades (iv) and its projected changes for the twenty-first century. Here, we assess the SWSA hydroclimate changes over the last century using observations, reanalyses and sets of 20 to 32 member-ensemble simulations conducted with the stand-alone LMDz6A-LR atmospheric component (Hourdin et al. 2020) and the IPSL-CM6A-LR coupled model (Boucher et al. 2020) as part of the 6th phase of the CMIP exercise (CMIP6; Eyring et al. 2016). The paper is organized as follows: in the next two sections, the data and methods used are introduced, the results obtained are presented in Sect. 4 and discussed in Sect. 5. A summary and the main conclusions are provided in Sect. 6.

## 2 Data

### 2.1 The atmospheric and coupled model

We used the CMIP6 version of the Institut Pierre-Simon Laplace (IPSL) stand-alone atmosphere model, called LMDz6A-LR (Hourdin et al. 2020) and the coupled atmosphere-ocean general circulation model (GCM), called IPSL-CM6A-LR (Boucher et al. 2020). LMDz6A-LR is coupled to the ORCHIDEE (d'Orgeval et al. 2008) land surface component, version 2.0. In IPSL-CM6A-LR, the LMDz6A-LR is coupled to the oceanic component Nucleus for European Models of the Ocean (NEMO), version 3.6, which includes other models to represent sea-ice interactions (NEMO-LIM3; Rousset et al. 2015) and biogeochemistry processes (NEMO-PISCES; Aumont et al. 2015). LR stands for low resolution, as the atmospheric grid resolution is 1.25° in latitude, 2.5° in longitude and 79 vertical levels

(Hourdin et al. 2020). Compared to the 5A-LR model version and other CMIP5-class models, IPSL-CM6A-LR was significantly improved in terms of the climatology, e.g., by reducing overall SST biases and improving the latitudinal position of subtropical jets in the SH (Boucher et al. 2020). The IPSL-CM6A-LR is also more sensitive to CO<sub>2</sub> forcing increase (Boucher et al. 2020) and represents a more robust global temperature response than the previous CMIP5 version consistently with current state-of-the-art CMIP6 models (Zelinka et al. 2020).

### 2.2 Experimental protocol

This study is based on a set of climate simulations generated as part of CMIP6 (Table 1). We relied on the pre-industrial control (piControl) coupled run with the external radiative forcing fixed to pre-industrial values for a measure of the internal climate variability generated by the IPSL-CM6A-LR model.

We also used the 32-member ensemble of simulations for the historical period (1850–2014), which is branched on random initial conditions from the piControl run to ensure that ensemble members are largely uncorrelated during the simulation. All 32 members of this ensemble (referred to as the historical ensemble) use the historical natural and anthropogenic forcings following CMIP6 protocol (Eyring et al. 2016). They include concentrations of GHGs from 1850 to 2014 provided by (Meinshausen et al. 2017) while the standard CMIP6 tropospheric and stratospheric ozone concentration were obtained from the Chemistry-Climate Model Initiative (Checa-Garcia et al. 2018). Tropospheric aerosols, from natural and anthropogenic sources (Hoesly et al. 2018; van Marle et al. 2017) are also included along with historical stratospheric natural forcings, corresponding to spectral solar irradiance-stratospheric ozone cycles (Matthes et al.

**Table 1** List of simulations with the IPSL-CM6A-LR model analyzed in the paper, the period covered, the size of the ensemble and imposed boundary conditions: observed SST, external forcing effects of GHGs, stratospheric ozone depletion, anthropogenic aerosols and natural forcings (namely stratospheric eruptions and spectral solar irradiance)

Name	Period	Ensemble size	Forcings				
			SST	GHG	Ozone	Aerosols	Natural
amip-hist	1870–2014	20	✓	✓	✓	✓	✓
historical	1850–2014	32	–	✓	✓	✓	✓
hist-GHG	1850–2014	10	–	✓	–	–	–
hist-O3	1850–20–2014	10	–	–	✓	–	–
hist-aer	1850–2014	10	–	–	–	✓	–
hist-nat	1850–2014	10	–	–	–	–	✓
piControl	1200 years	1	–	–	–	–	–
ssp585	2015–2100	6	–	✓ <sup>a</sup>	✓ <sup>a</sup>	✓ <sup>a</sup>	✓ <sup>a</sup>
ssp126							

<sup>a</sup>The forcing values in the ssp585 and ssp126 future projections are set according to the homonymous scenario of socio-economic development, while the rest of simulations include external forcings that are consistent with observations since 1850

2017) and the main volcanic eruptions prescribed with the aerosol optical depth (Thomason et al. 2018).

Detection and attribution 10-member ensembles (Gillett et al. 2016) are also utilized to understand the role of the different external forcing components in the context of climate change. These experiments are equivalent to the historical ones but include each forcing individually namely either GHGs (hist-GHG), stratospheric ozone depletion (hist-stratO3), aerosols (hist-aer) and natural (hist-nat) while maintaining other forcing at their 1850 level.

Two 6-member ensembles for the twenty-first century (2015–2100) future projections scenarios branched on randomly selected historical members at the year 2014 are also analyzed (O'Neill et al. 2016): the ssp585 equivalent to  $\sim 8.5 \text{ W m}^{-2}$  increased radiative forcing in the year 2100 due to GHG emissions (the highest future pathway across all CMIP6 scenarios) and the ssp126 mitigation scenario, which assumes the lowest of plausible radiative forcing effects ( $2.6 \text{ W m}^{-2}$ ) in 2100 assuming substantial mitigation against global warming.

Finally, we also use AMIP historical (amip-hist) simulations, which use the same external forcings since 1870 as the historical experiment but with imposed observed monthly SST on the LMDz6A-LR atmospheric component. Further details about external forcings implementation strategies in the experiments mentioned above are given in Lurton et al. (2020).

### 2.3 Observational data

In addition to model outputs, different observational products are used: in situ and gridded observations data sets and reanalyses (Table 2). We analyze in situ monthly precipitation data from 1960 to 2017 from rain gauges in 129

stations located along the Andes, between  $70^{\circ}$ – $73^{\circ}$ W and  $20.5^{\circ}$ – $46.5^{\circ}$ S provided by the Chilean Center for Climate and Resilience Research, Climate Explorer (<http://explorador.cr2.cl>) (Fig. 1). Note that the station coverage is relatively sparse outside the  $27^{\circ}$ – $43^{\circ}$ S region in SWSA. We also rely on gridded products of monthly precipitation provided by the Global Precipitation Climatology Centre (version 2018; GPCCv2018) and the University of Delaware Air Temperature and Precipitation (version 5.01; UDEL5.01), each of which using different interpolation methods. Note in Fig. 1 that the data coverage of the observations used for the reconstruction of these gridded products is consistent with that of the in situ observations, which are quite sparse outside SWSA in southern South America.

We use the Hadley Centre Sea Ice and Sea Surface Temperature version 1 (HadISST) gridded reconstruction of SST observations, which are used as boundary conditions in the LMDz6A-LR model amip-hist CMIP6 simulations. To study the atmospheric dynamics, we also analyze the meridional wind and the surface pressure variables from several reanalyses: the NOAA-CIRES 20th Century Reanalysis versions 2 (20CRv2), 2c (20CRv2c) and 3 (20CRv3), the ERA-20C, ERA40 and ERA-Interim reanalyses of the European Centre for Medium-Range Weather Forecasts and the National Center for Environmental Prediction (NCEP) and the National Center for Atmospheric Research (NCAR) reanalysis version 1 (NCEP1) and 2 (NCEP2).

**Table 2** List of observations and reanalyses used in our analyses

Variable	Data base	Data type	Resolution ( $^{\circ}$ lat $\times$ $^{\circ}$ lon $\times$ vertical levels)	Period	References
Precipitation	CR2	Rain gauge	In situ	1960–2017	<a href="http://www.cr2.cl">http://www.cr2.cl</a>
	GPCCv2018	Gridded	$0.5^{\circ} \times 0.5^{\circ}$	1891–2016	Schneider et al. (2018)
	UDEL5.01			1900–2017	Willmott and Matsuura (2001)
SST	HadISST1	Gridded	$1^{\circ} \times 1^{\circ}$	1870–2015	Rayner et al. (2003)
SLP	HadSLP2	Gridded	$5^{\circ} \times 5^{\circ}$	1850–2017	Allan and Ansell (2006)
Wind and surface pressure	NOAA-CIRES 20CR-V2	reanalysis	$2^{\circ} \times 2^{\circ} \times 24$	1871–2010	Compo et al. (2011)
	NOAA-CIRES 20CR-V2c		$2^{\circ} \times 2^{\circ} \times 24$	1851–2014	
	NOAA-CIRES 20CR-V3		$1^{\circ} \times 1^{\circ} \times 64$	1836–2015	Slivinski et al. (2019)
	ERA-20C		$2^{\circ} \times 2^{\circ} \times 37$	1900–2010	Poli et al. (2016)
	ERA-40		$1.1^{\circ} \times 1.1^{\circ} \times 23$	1970–20–2001	Uppala et al. (2005)
	ERA-Interim		$0.75^{\circ} \times 0.75^{\circ} \times 37$	1979–2017	Dee et al. (2014)
	NCEP1		$2.5^{\circ} \times 2.5^{\circ} \times 17$	1948–2017	Kalnay et al. (1996)
NCEP2	$2.5^{\circ} \times 2.5^{\circ} \times 17$	1979–2017			



## 3 Methods

### 3.1 Trend analyses and statistical testing

All anomalies are calculated by removing the monthly mean seasonal cycle of the entire covered period (Table 1) from the time series before calculating seasonal averages (MAM, JJA, SON and DJF). To focus only on the variability from decadal, interdecadal or longer time scales, time series are low-pass filtered (LPF) using a Butterworth filter with a cut-off period of 8, 13 or 40 years, respectively (Butterworth 1930). The linear trend for each month over 1979–2014 is obtained by applying least squares on unfiltered yearly time series of monthly mean precipitation and represented in terms relative to the climatological mean (% decade<sup>-1</sup>). In this case, trend values are statistically tested with a Student *t*-test with the number of degrees of freedom corresponding to the total number of years minus one. To evaluate the ensemble-mean trend representativeness, we also indicate the regions where at least 80% of the members display trends of the same sign than the ensemble mean. The consistency between the anomalies of the climate parameters and the modes of variability was estimated using the regression coefficient ( $\alpha$ ) between these variables. When the time series are spatially distributed the resulting regression coefficients are presented as regression patterns. In this case, the ensemble-mean regression coefficients are statistically tested using a random-phase test, based on Ebisuzaki (1997), adapted to the regression (details in Villamayor et al. 2018). In turn, the level of uncertainty among individual members is indicated by showing the grid points, where at least 80% of them display a regression coefficient of the same sign as the ensemble mean. When considering regionally averaged time series for the ensemble mean, the uncertainty of the resulting regression coefficient is quantified by representing the range of values obtained with all members individually.

### 3.2 Climate indices

We consider five main sets of climate indices that are introduced below. Note that for ensemble simulations, the ensemble-mean index refers to the indices calculated from outputs previously averaged across all members. The 95% confidence interval among individual members, according to a Student *t*-test, is shown to quantify the uncertainty of the ensemble-mean indices.

#### 3.2.1 SWSA precipitation indices

Empirical Orthogonal Function analysis of the 8-year LPF rainfall anomalies in southern South America (25°–58°S, 65°–80°W) is performed to isolate the leading mode of variability at decadal-to-longer time scales. The first Principal

Component (PC1) for each season is standardized to get a measure of the variance. Regions with the highest variance are then used to build regional indices by averaging values over: 34°–49°S, 71°–77°W in MAM; 28°–40°S, 70°–76°W in JJA; 30°–43°S, 70°–77°W in SON and 39°–50°S, 72°–78°W in DJF.

#### 3.2.2 Global warming and IPO sea surface temperature indices

A global warming index (GW) is calculated by spatially averaging 40-year LPF annual-mean SST anomalies (SSTAs) over 45°S–60°N. Residual SSTAs are then derived by regressing out the GW SSTAs pattern. To analyze the IPO influence on SWSA rainfall, an IPO index is computed using the residual SSTA following the tripole approach of Henley et al. (2015), defined as the central equatorial Pacific SST (10°S–10°N, 170°E–90°W) minus the average of northwest (25°–45°N, 140°E–145°W) and southwest (15°–50°S, 150°E–160°W) Pacific SST. The resulting IPO index is then LPF with a 13-year cut-off period.

#### 3.2.3 Southern Annular Mode and Hadley Cell extent indices

Seasonal SAM indices are computed for each season as the standardized PC1 of the 8-year LPF sea level pressure (SLP) anomalies in the SH, south of 20°S. In order to describe the variability of the latitudinal position of the poleward edge of the HC in the SH, we define an index of the HC extent (HCE) for each season as the linearly interpolated latitude for which the 500-hPa meridional streamfunction ( $\psi_{500}$ ) is equal to zero between 20° and 40°S.

### 3.3 Decomposition of SWSA precipitation variance

A decomposition of the variance of SWSA precipitation into the components explained by the IPO and the GW SST indices is performed based on a multilinear regression analysis (Mohino et al. 2016). According to this, the total variance of SWSA precipitation ( $\text{var}[PR]$ ) can be expressed in terms of the regression coefficients from the multilinear fitting that correspond to each index ( $\alpha_{IPO}$  and  $\alpha_{GW}$ , respectively) and a residual ( $\text{var}[\epsilon]$ ) as follows:

$$\text{var}[PR] = \alpha_{IPO}^2 + \alpha_{GW}^2 + \text{var}[\epsilon] \quad (1)$$

The residual term stands for the variance of the residual of the multilinear fitting, namely the variance that cannot be explained by the IPO and the GW indices. These three components are expressed as percentage of the total variance of SWSA precipitation.

### 3.4 Total moisture budget decomposition

A decomposition of the change in the net moisture budget, expressed as precipitation minus evaporation ( $P-E$ ), into purely thermodynamic and dynamic components is performed in this work. According to the moisture budget equation,  $P-E$  equals the divergence of the moisture flux (Brubaker et al. 1993). The moisture flux is the mass-weighted and vertical integral of the product between the specific humidity ( $q$ ) and the horizontal winds ( $\mathbf{u}$ ). Therefore, a change in  $P-E$  ( $\delta(P-E)$ ) implies changes in  $q$  (i.e., thermodynamic changes ( $\delta TH$ )) and  $\mathbf{u}$  (i.e., dynamic changes ( $\delta DC$ )). Considering such a change as an anomaly with respect to a reference period (denoted with subscript  $r$ ), the thermodynamic and the dynamic components can be separated using the following approach (Seager et al. 2010):

$$\delta(P-E) = \delta TH + \delta DC + RES \quad (2)$$

Following Ting et al. (2018), we define  $\delta TH$  and  $\delta DC$  as follows:

$$\delta TH \approx -\frac{1}{g\rho_w} \cdot \nabla \int_0^{p_s} \mathbf{u}_r \cdot \delta q \, dp \quad (3)$$

$$\delta DC \approx -\frac{1}{g\rho_w} \cdot \nabla \int_0^{p_s} \delta \mathbf{u}_r \cdot q \, dp, \quad (4)$$

where  $g$  is the gravitational acceleration,  $\rho_w$  the density of water,  $p$  pressure levels and  $p_s$  the surface pressure.

The residual component ( $RES$ ) mostly accounts for the moisture convergence changes due to transient eddies, but also includes nonlinear terms that are typically neglected in the approach of  $\delta TH$  and  $\delta DC$  (Seager et al. 2010; Ting et al. 2018).

### 3.5 Probability density functions of precipitation linear trend

To further evaluate the role of the IPO phase shift (such as during the 1979–2014 period) on SWSA precipitation trends in our model as compared to observations, we performed Probability Density Functions (PDFs) of the linear trend of SWSA precipitation for 36-year periods separately for ensemble members with a positive or negative IPO trend that is significant at the 5% level during the period (resulting in 25 members of each category). The two resulting PDFs are statistically compared by testing the null hypothesis that both present independent normal distributions with equal means and equal but unknown variances at the 20% significance level, according to a  $t$ -test. A  $t$  test is also used to

evaluate whether mean trend values are significantly different from zero.

## 4 Results

### 4.1 Model validation

In this section, we present a comparison of the amip-hist and historical simulations with observational products to evaluate the ability of, respectively, the atmospheric component and the coupled model to simulate main aspects of precipitation in SWSA, such as climatology and tendency. We also check simulated IPO phase shifts and the emerging HC expansion, which are addressed in relation to the recent drying trend in SWSA.

#### 4.1.1 SWSA precipitation

The SWSA region rainfall annual cycle over the period common to observations and simulations (1960–2014) is represented in Fig. 2 (left panel). Considering the spatial coverage of observations in SWSA (Fig. 1), the model validation is restricted to a latitudinal band between 20° and 47°S. This band is roughly 5° longitude width (i.e., two grid points in the model) and centered in 73.75°W. Most of the rain gauge stations are located in the west Chilean territories adjacent to the Andes where precipitation is enhanced by the orographic blocking effect on the westerly atmospheric flow (Falvey and Garreaud 2007; Smith and Evans 2007; Viale et al. 2019). The rain gauge observed annual cycle shows a latitudinal migration of rainfall sustaining marked dry and wet seasons in austral summer (DJF) and winter (JJA), respectively (Fig. 2a). The onset of the rainy season occurs gradually during fall (MAM), with maximum rainfalls registered around 37°S in June. This regional maximum is not well captured by the gridded observations, most likely because of interpolation procedures applied to rain gauge data (Fig. 2c and e). The rainy season demise occurs in spring (SON), before minimum values are reached in summer.

The amip-hist and historical simulations reproduce the observed mean annual cycle, with the onset in MAM, the rainy season in JJA with a maximum in June around 37°S, the demise in SON and the dry season in DJF (Fig. 2g and i). The model seems to overestimate climatological values north of 35°S and south of 40°S. This discrepancy may instead be attributable to the lack of observations at these latitudes. There is also a high level of uncertainties in observations regarding the climatological amount. Annual rainfalls reach around 1460 mm in rain gauge observations where it is most rainy between 35°S and 40°S, while gridded products values are about two thirds of this amount (i.e., 910 mm in GPCCv2018 and 890 mm in UDEL5.01). Model

ensemble-means for amip-hist and historical simulations amount 1670 and 1450 mm respectively, with an ensemble standard deviation of around 25 mm in both cases, which is close to in situ observations. However, historical simulations generally give smaller values than amip-hist, especially during the rainy season. This difference is independent of the size of both ensembles (not shown) and most likely related to the influence of the observed SSTs in amip-hist runs.

The annual cycle of the linear trend relative to the climatological mean over the last 36 years (1979–2014) is represented in Fig. 2 (right panel). A significant drying around 33°–40°S in April–May and around 29°–36°S in July is observed consistently in all observations datasets (Fig. 2b, d, f). These drying trends indicate a delay in the onset of the rainy season and less rainfall during the rainy season. Although weak and not significant, negative trend values in September, together with the features described before, suggest that, in general, there is a tendency towards shorter and less effective rainy season in SWSA over the last decades. The Hövmoller diagrams from gridded observations show positive trend during late spring and summer south of 40°S, suggesting that the southernmost part of SWSA has become wetter (Fig. 2d and f). However, this result is poorly reliable due to the lack of observations in this part of the Andes (Fig. 1).

Both amip-hist and historical simulations indicate a widespread drying relative to the simulated climatology along the year, with a maximum from around ~ 40°S in DJFM to ~ 27°S in MJJAS (Fig. 2h and j), suggesting a shortening and weakening of the rainy season. The drying trend is in general stronger in amip-hist simulations than in historical runs (independently of the ensemble size, not shown). All amip-hist members include the same observed SST, while in historical simulation, SST variability is largely uncorrelated among ensemble members. Averaging the historical ensemble allows therefore damping the influence of SST on the simulated rainfall trends with respect to the role of external forcing. Differences with amip-hist on the other hand, emphasize the contribution of observed SST variability. The drying trend during the onset and demise of the rainy season is more intense and significant in the amip-hist ensemble mean than in the historical one. This suggests a dominant role of observed SST variability (such as the shift toward a negative IPO) in the rainy season shortening during 1979–2014, probably amplified by external forcing influence.

To summarize, despite the constraints of comparing local observations with gridded data from GCMs due to the complex orography of the region, the model can reproduce the main observed rainfall climatological features and recent trends. Differences between the amip-hist and the historical coupled simulations suggest a combination of internal and external factors in driving the SWSA

drying trend. Previous generation CMIP5 models show an overall underestimation of the SWSA precipitation response to external forcing (Vera and Díaz 2015; Boisier et al. 2018) that is coherent with the IPSL-CM6A-LR simulations. On the other hand, a preliminary CMIP6 multi-model study places the IPSL-CM6A-LR among the GCMs that best represent the atmospheric changes over southeast Pacific that modulate SWSA rainfall during the last century (Rivera and Arnould 2020), which supports the use of this model to study the long-term precipitation variability in this region.

#### 4.1.2 IPO phase shifts

We also evaluate the model ability to simulate IPO phase shifts comparable to the observed shift over the 1979–2014 period addressed by Boisier et al. (2016) in terms of the amplitude of the associated SST anomalies. To this aim, Fig. 3 represents IPO indices from observational data (Had-ISST1) over 1870–2014 and from the piControl run over a representative period of equal length, as well as the linear trend values obtained along both IPO indices in centered running windows of 15–40 years long. The trend graphics show blue and red colored plumes, corresponding to negative and positive trend values, respectively. The plumes resulting from the piControl IPO index are, in general, narrower than those from observations. This reveals that the model underestimates the observed persistence of the IPO phases. However, the model succeeds in simulating 36-year IPO phase shifts of up to  $-0.2$  °C per decade comparable to the one observed over 1979–2014.

#### 4.1.3 Hadley Cell expansion

To evaluate the model's ability to reproduce the HC expansion in recent decades, we compare the linear trend of the seasonal HCE indices calculated with eight different reanalyses and the amip-hist and historical simulations for their common 23-year period (1979–2001) and for a 40-year period (1971–2010), common to the simulations and five reanalyses (Fig. 4). The trend values obtained over the short period show large dispersion between the different members of the amip-hist and historical simulations, compared with those of the longer period. This shows the dependence of the tendency of the HCE index on short-term stochastic internal variability. In the longer term, the trend is more robust across model members suggesting an influence of external forcings. Comparing across seasons, the simulated HCE trend is better constrained among members in JJA and most uncertain in DJF, when the HC is most variant and presents wider expansion. Regarding observations, the trend values obtained from reanalyses show large spread as well. Despite the large uncertainty, when the 40-year long period

is considered, there is solid agreement among reanalyses regarding the Southern HC expansion towards the pole in recent decades (Grise et al. 2019).

The model simulates trends that are within the range of those in the reanalyses. The trend of the simulated HCE in the ensemble mean is negative in all seasons and in both amip-hist and historical simulations, being widest in DJF. In MAM, the poleward expansion of the HCE is the weakest and close to zero when simulated by the historical simulation, while the amip-hist simulation shows a broader expansion. In contrast, during the other seasons, the simulated ensemble-mean expansion is similar in both simulations, being wider in the historical over the 40-year-period. These results suggest that the external forcing mostly induces the HC poleward expansion in JJA, SON and particularly in DJF, but in MAM this effect is weak and, presumably, the influence of SST internal variability is also relevant.

#### 4.2 Relative roles of forced versus internal variability on SWSA precipitation decadal variability and trend

In this subsection, we focus on the amip-hist ensemble to unravel the contribution of observed SST to SWSA precipitation low-frequency variability. The first PCs of the 8-year LPF seasonal precipitation anomalies account for much of the total decadal-scale rainfall variability in southern South America (25°–58°S; 65°–80°W). The explained total variance of the PC1 is 59.1% in MAM, 75.7% in JJA, 67.0% in SON and 69.9% in DJF. These indices together with their respective regression patterns show that most of the precipitation variability in southern South America is concentrated in a dipole of opposite anomalies between the middle (25°–45°S) and high (>50°S) latitudes in SWSA (Fig. 5). The seasonal patterns in DJF and MAM also present significant anomalies in subtropical South America east of the Andes showing an opposite sign to those recorded in middle SWSA latitudes.

These regression patterns allow identifying where the most substantial low-frequency variability occurs in the amip-hist simulations (boxed areas in Fig. 5). These regions vary depending on the season, showing a north-to-south shift from winter (JJA) to summer (DJF), respectively, and are co-located with the centers of maximum rainfall linear trends (gray contours in Fig. 5). These regions with the most substantial negative rainfall anomalies are associated with PC1s positive long-term trend (Fig. 5, left panels), which accounts for nearly the total tendency of the area-averaged precipitation anomalies for each season (Table 3). From 1970 to 2014 a deficit of 6.2 mm per decade and around 15.2 mm per decade is simulated for the rainy (JJA) and dry summer (DJF) seasons respectively.

**Table 3** Ensemble-mean 1970–2014 linear trend in mm decade<sup>-1</sup> of the amip-hist precipitation ( $\delta$ ) and of the precipitation anomalies coherent with the corresponding PC1 index ( $\delta_{PC1}$ ) averaged over the boxed areas in Fig. 5

	MAM	JJA	SON	DJF
$\delta$	– 8.54	– 6.18	– 6.31	– 15.15
$\delta_{PC1}$	– 8.04	– 5.45	– 5.17	– 15.81

All values are significant with 95% confidence interval

Previous studies have shown evidence for the influence of SST internal variability and external forcings on SWSA rainfall recent changes (e.g., Boisier et al. 2016, 2018). In line with these previous works and to identify potential connections between simulated low-frequency variations of SWSA precipitation and observed internal modes of climate variability, we regress PC1s on anomalies of SST, SLP and wind (Fig. 6) before and after removing the long-term trend signal in PC1s with a 3rd-degree polynomial fit (dotted lines in Fig. 5). Such detrending will allow emphasizing typical SST and teleconnection patterns related to internal variability modes.

Without detrending, SST regression patterns show warm anomalies almost globally distributed except in the tropical Pacific where an IPO-like relative cooling dominates all year round (left panel in Fig. 6). The warm pattern is most widespread in DJF, with strong anomalies over western Pacific, the Indian and Atlantic Oceans, especially in the southern basin, and weakest in JJA. In turn, the tropical Pacific cooling is more intense in SON and JJA and almost negligible in DJF and MAM. This global SST pattern is reminiscent of an IPO negative phase combined with the global warming signal induced by external forcing. In DJF and MAM surface winds and SLP anomalies show a poleward shift of the westerlies and a SLP maximum slightly south of 30°S associated with the SWSA drying. This suggests a link with the strengthening of the SAM with a weaker influence of the negative IPO pattern on the SWSA drying in austral summer and fall, in agreement with Boisier et al. (2018).

Regression patterns obtained with the detrended PC1s highlight a sea-level pressure high and significant anomalous easterlies in Southeastern Pacific in JJA and SON, suggesting an atmospheric teleconnection with a negative IPO-like SSTA pattern most prominent in austral winter and spring (right panel in Fig. 6). Extratropical SLP anomalies are less zonally symmetric than with the non-detrended PC1s with an anomalous jet of westerlies passing through SWSA south of around 45°S, which is coherent with the anomalous SLP gradient. Therefore, this pattern may suggest that, in response to a negative IPO, there is a poleward shift of the storm-tracks embedded in the zonal flow (Garreaud et al. 2013), resulting in less intrusion of humid air masses over middle latitudes in SWSA. Comparison of regression



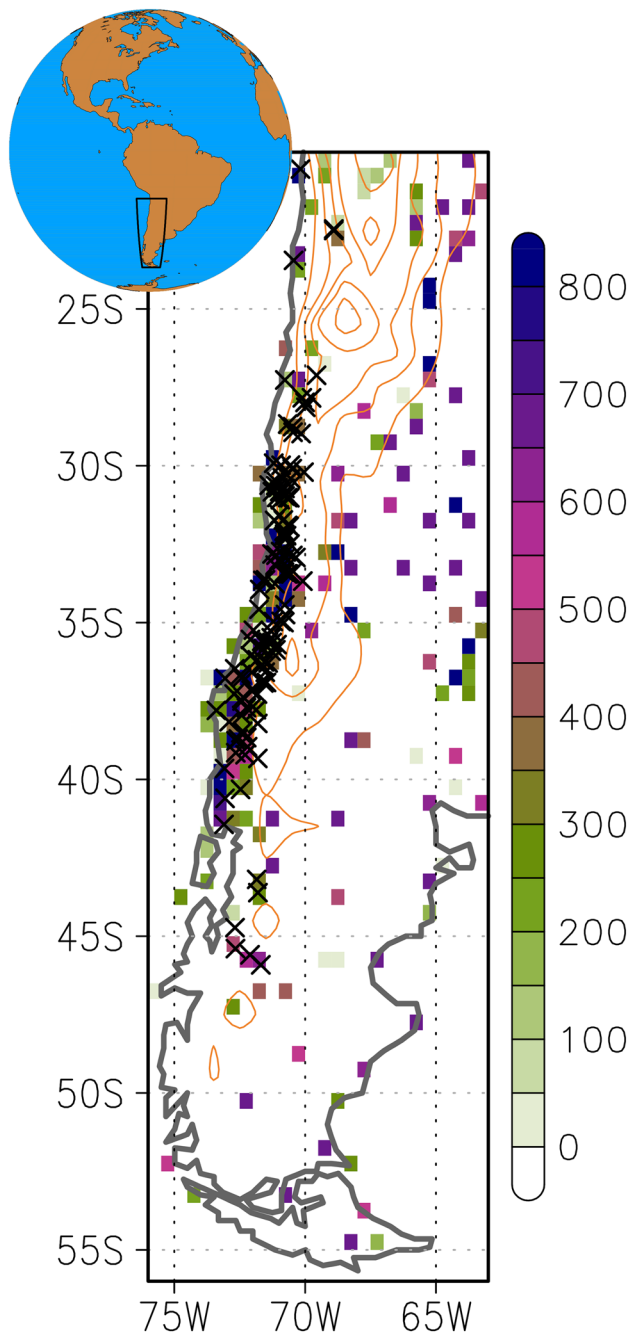


**Fig. 1** Details of in situ precipitation observations in South Western South America (SWSA). Crosses: location of the 129 rain gauge stations of the observations used. Colored boxes: number of observed rainfall monthly data accumulated over 1960–2014 at 0.5° horizontal resolution in GPCCv2018. Orange contours: altitude levels in 1000-m intervals

patterns before and after PC1s detrending indicates therefore that precipitation trends in winter (JJA) and spring (SON) are largely influenced by internal IPO related SST variability (Boisier et al. 2016). On the other hand, high-latitude atmospheric circulation associated with the SST warming signal

dominates SWSA rainfall trends especially in summer (DJF) and fall (MAM) (e.g., Boisier et al. 2018).

To further evaluate the respective roles of the global warming and internal SST variability on SWSA precipitation, a multilinear regression analysis over 1870–2014 is performed using as predictands the simulated seasonal indices of SWSA precipitation (i.e., area-weighted mean over boxed areas in Fig. 5) and the IPO and GW observed SST indices as predictors (Fig. 7). The results show that the IPO barely explains 19% and 15% of the precipitation low-frequency total variance in JJA and SON, respectively, and that its contribution is almost null in MAM and DJF (Fig. 7). The GW index explains a larger proportion of rainfall variance in all the seasons except in JJA. The external forcing influence is exceptionally remarkable in DJF, where the GW dominates the precipitation variance above the IPO, which shows very little impact. However, the explained variance by the GW index only represents the indirect external forcing influence on SWSA rainfalls through induced SST anomalies. It does not account for the externally forced changes in atmospheric dynamics and direct thermodynamic effects in SWSA. The fact that the residual component is considerably large in all seasons suggests that SST changes are not a significant driver of the SWSA precipitation variability at decadal-to-longer time scales.

A possible explanation for the low response of the simulated SWSA precipitation to the IPO could be due to the unrealistically weak atmospheric teleconnection simulated by the model. However, the SLP anomalies regressively associated with the IPO in JJA over southeastern Pacific (blue box in Fig. 6b) in HadSLP2 observations (0.24 hPa per standard deviation) lies within one standard deviation of the ensemble-mean values of the amip-hist and historical simulations (respectively,  $0.32 \pm 0.14$  and  $0.34 \pm 0.15$  hPa per standard deviation). Hence, we cannot attribute the relatively weak influence of the internal SST decadal variability on simulated rainfall to insufficient sensitivity of the atmospheric component of the model to SST anomalies.

The SWSA precipitation response to the IPO simulated in amip-hist, historical and piControl simulations (see Table 1) are shown in the bottom panel of Fig. 7. MAM and DJF rainfall responses are positive in the amip-hist and historical ensembles, but weak and not emerging from the internal variability as represented by the piControl simulation. In turn, this positive signal is significant in amip-hist in JJA and SON, the strongest being in JJA. In the historical simulations, the response to the IPO is also positive and strongest in JJA but not significant as in all seasons, consistently with the unforced piControl run. These observations suggest that the difference in the SWSA response to IPO between forced and unforced coupled model simulations is not significant. Therefore, according to these results, it can be inferred that the IPO can impact on the simulated SWSA precipitation.



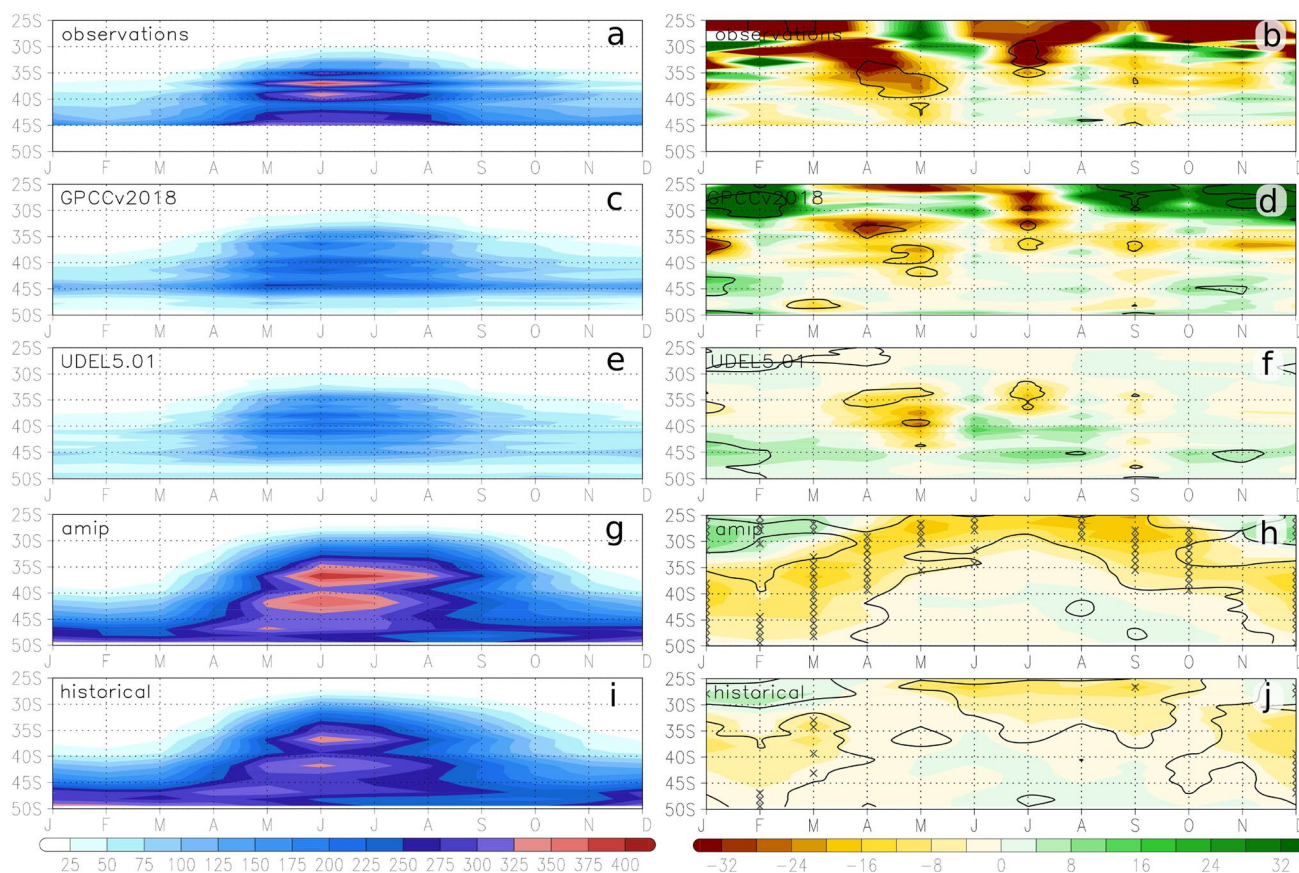


**Fig. 2** Hövmoller diagrams representing the climatological annual cycle of monthly precipitation averaged over 1960–2014 (left panel; units are mm) and the linear trend over 1979–2014 (right panel; units are % decade<sup>-1</sup>) averaged across 75°–70°W from **a, b** the rain gauge observations linearly interpolated to a regular grid of 1° latitude, **c, d** the GPCCv2018 and **e, f** UDEL5.01 gridded observations, **g, h** from

the ensemble-mean amip-hist and **i, j** historical simulations. Crosses in **h, j** indicate where the trend in 80% of the simulation members show the same sign as the ensemble-mean. Contours in right panel indicate the trend significance at the 5% level according to a Student *t* test with number of years minus one degrees of freedom

Still, its influence is weak as compared to external forcing and only robustly reproducible with the SST-forced amip-hist simulations in JJA and, to a lesser extent, in SON. Next, we examine the relative influences of dynamical and thermodynamical external forcings on the low-frequency variability and trend of SWSA rainfalls.

### 4.3 Role of dynamical vs. thermodynamical changes in SWSA

In the previous subsection, anomalous poleward shift of the zonal circulation in high-latitudes in the SH is attributed to external forcings. This suggests that external forcings act on SWSA precipitation through dynamical changes. However, it has been shown that long-term dynamical changes cannot account for all the externally forced trend in subtropical precipitation with direct thermodynamic effects playing an important role (Schmidt and Grise 2017). Therefore, the question arises as to whether the forced component of

precipitation in SWSA is mostly induced by dynamic or thermodynamical processes. To shed light on the leading process, we express the change in the net surface moisture budget as the difference of precipitation minus evaporation ( $P-E$ ) over 2005–2014 versus 1851–1910 ( $\delta(P-E)$ ). Besides, we decompose  $P-E$  into a thermodynamic component ( $\delta TH$ ), due to changes in the specific humidity, a dynamic component ( $\delta DC$ ) due to changes in circulation, and a third component associated with transient eddies (Seager et al. 2010). The change of the annual mean  $P-E$  obtained from the ensemble-mean historical simulations roughly presents a hemispheric pattern that represents the “wet gets wetter and dry gets drier” paradigm of Held and Soden (2006) (Fig. 8a). It is worth noting that the deficit of moisture supply in SWSA stands out across other extratropical continental regions of the SH. The decomposition of the change of seasonal moisture supply (Fig. 8b), reveals that changes in the atmospheric circulation account for a large share of the total change compared to the direct thermodynamic effects

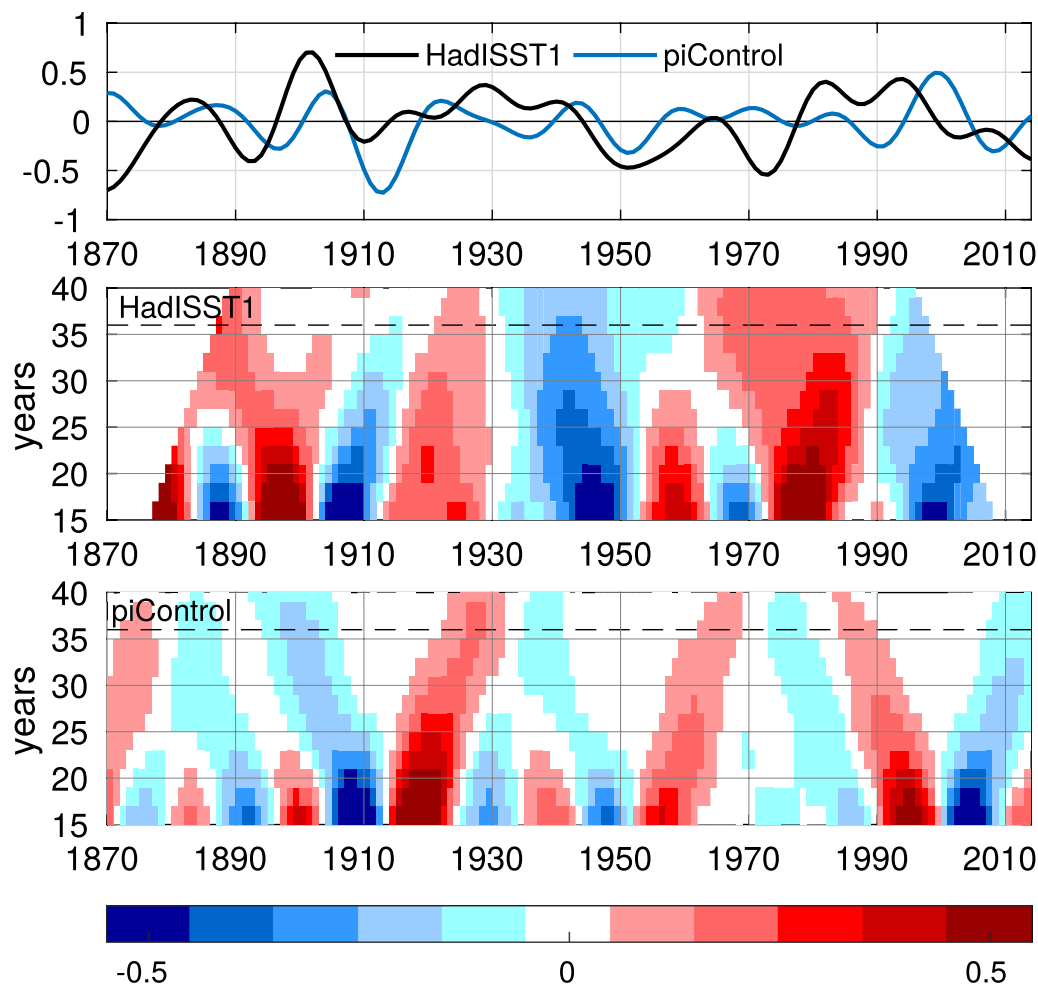


**Fig. 3** Observed and simulated amplitude and persistence of the Interdecadal Pacific Oscillation Index (IPO) phase shifts. Upper panel: IPO indices from (black) HadISST1 observations over 1870–2014 and (blue) the piControl run over an equivalent 145-year period. Mid-

dle (bottom) panel: Trend values in units of °C per decade of the HadISST1 (piControl) IPO index in centered running windows of varying periods of 15-to-40 years (y axis). Dashed horizontal line indicates the 36-year running window equivalent to the 1979–2014 period

of external forcing in all seasons. Consistent with these findings, in the next section, we examine the potential large-scale dynamics sources associated with the induced SWSA drying.

#### 4.4 Connections between the HCE, SAM and SWSA rainfall

An anomalous shift of the circumpolar circulation in the SH high-latitudes, like the one shown by the regression patterns of the undetrended PC1s of SWSA precipitation on circulation forcings (Fig. 6), has been related to a persistent positive SAM trend and a widening of the HC in response to external forcings (e.g., Gillett and Thompson 2003; Amaya et al. 2018). The historical ensemble mean shows that the seasonal low-frequency indices of SWSA precipitation, HCE and SAM describe a consistent trend (left panel in Fig. 9; note

that the SAM indices are reversed). This trend is stronger since ~1970s and more pronounced in DJF and MAM than in JJA and SON. The square of the correlation coefficient ( $R^2$ ) reveals high co-linearity among the three indices in all seasons (right panel in Fig. 9). SWSA precipitation is almost equally correlated to HCE and SAM, showing the highest co-linearity in DJF ( $R^2 = 0.87$  and  $R^2 = 0.92$ , respectively) and the lowest in JJA ( $R^2 = 0.73$  and  $R^2 = 0.74$ , respectively). In turn, the HCE and the SAM also show a strong co-linearity between each other that is strongest in DJF ( $R^2 = 0.95$ ) and weakest in JJA ( $R^2 = 0.86$ ). This result suggests that both dynamical large-scale atmospheric modes vary in synchronously and modulate SWSA precipitation in the same direction in response to external forcings. Since both HCE and SAM are highly co-linear, we next focus only on HCE index to investigate and attribute the simulated trends.

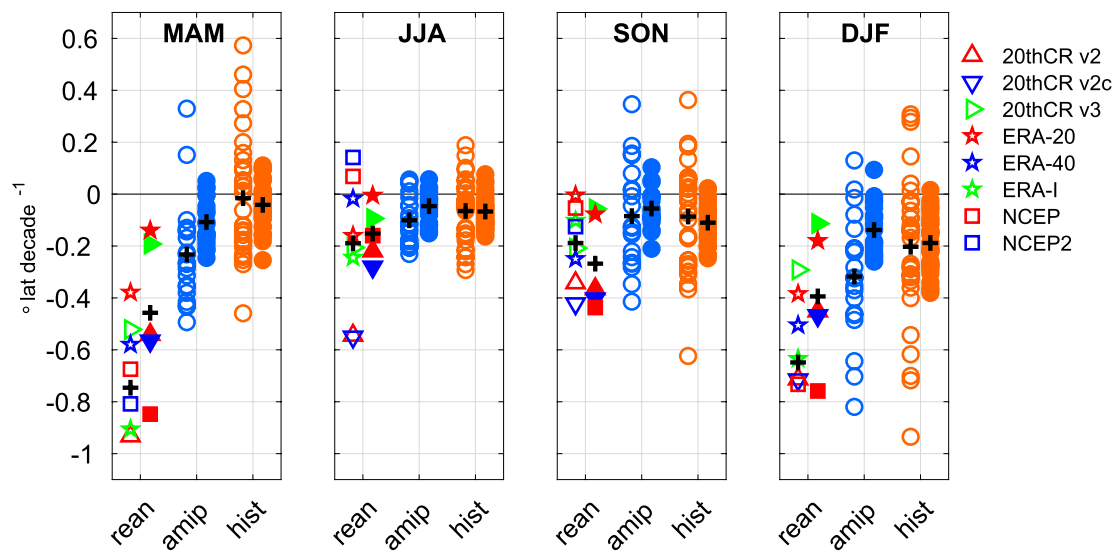


**Fig. 4** Linear trend of the seasonal HCE index, expressed in latitude degrees per decade, obtained with reanalyses (*rean*; left column) and all members of the amip-hist (*amip*; blue circles) and the historical (*hist*; orange circles) simulations. Empty shapes correspond to the

trend along the common period among all data used (1979–2001) and filled ones to a longer period of 40 years (1971–2010). Black crosses indicate the trend value averaged across all reanalyses or ensemble members

#### 4.5 Attribution of forced variability

Until the early 1970s, the HCE indices of all coupled simulation oscillate around the piControl climatological value and within the threshold of internal variations in all seasons (Fig. 10, left panel). Afterwards, the historical ensemble-mean indices show a poleward expansion in all seasons, even exceeding the bounds of internal variations by the 2000s in JJA, SON and DJF. At the same time, the hist-nat experiment simulates no appreciable change of the HCE variability. Such tendencies evidence the role of the anthropogenic forcings on the recent HC expansion.

To highlight the role of external forcings, the linear trend over 1970–2014 of the ensemble-mean HCE indices is analyzed (Fig. 10, middle panel). The trend displayed by the historical simulation is negative, denoting a poleward expansion, and significantly different from zero (with 99% confidence interval) in all seasons, being even robust among all members in DJF. The expansion is widest in this season with a trend of  $-0.20^{\circ}$  lat per decade, then  $-0.04^{\circ}$  lat per decade in MAM,  $-0.07^{\circ}$  lat per decade in JJA and  $-0.11^{\circ}$  lat per decade in SON. Large error bars evidence the great influence of internal weather noise. GHG forcing alone has a large effect all year round, with a signature that emerges out of the internal noise by the early 2010s in MAM and the 2000s in JJA and SON, with significant 1970–2014 linear trends of  $-0.06$ ,  $-0.09$  and  $-0.10^{\circ}$  lat per decade, in the respective seasons. Such trend values highlight the leading role of GHGs in the HC expansion during these seasons. In DJF, instead, the stratospheric ozone depletion leads the HC

expansion, inducing wider shift ( $-0.11^{\circ}$  lat per decade) than GHGs ( $-0.06^{\circ}$  lat per decade) separately. Anthropogenic aerosols (aer) induce a significant HCE equatorward shift in JJA ( $0.02^{\circ}$  lat per decade) and SON ( $0.06^{\circ}$  lat per decade) from around the mid-1990s with a peak in the mid-2000 and a partial recovery afterwards. Nevertheless, this contraction is constrained within the threshold of internal variability. The 1970–2014 linear trend of the “sum” index, obtained by adding the ensemble-mean HCE anomalies from individual forcings, is significantly close to the historical one (with 95% confidence interval) in DJF, MAM and JJA. Therefore, the effects of the external forcings are, overall, additive all year round, except in SON due to the influence of anthropogenic aerosols that tends to offset the trend of the “sum” index ( $-0.04^{\circ}$  lat per decade) respectively to historical experiments ( $-0.11^{\circ}$  lat per decade).

To quantify the role of the HCE in the forced SWSA drying over 1970–2014, we represent the total trend of SWSA precipitation from the ensemble-mean simulations and the HCE-coherent trend in Fig. 10 (right panel). The historical experiment shows a precipitation reduction of 4.5, 4.4, 3.6 and 10.3 mm per decade in MAM, JJA, SON and DJF, respectively, in response to all external forcings. The HCE-coherent trend underestimates by 40% the total drying in MAM. Still, it shows no significant difference with the total trend in the other seasons, which highlights the overall leading role of the HC expansion on the drying trend induced by external forcing. In MAM, in response to only GHGs the total precipitation trend is significantly similar to the one induced by all forcings

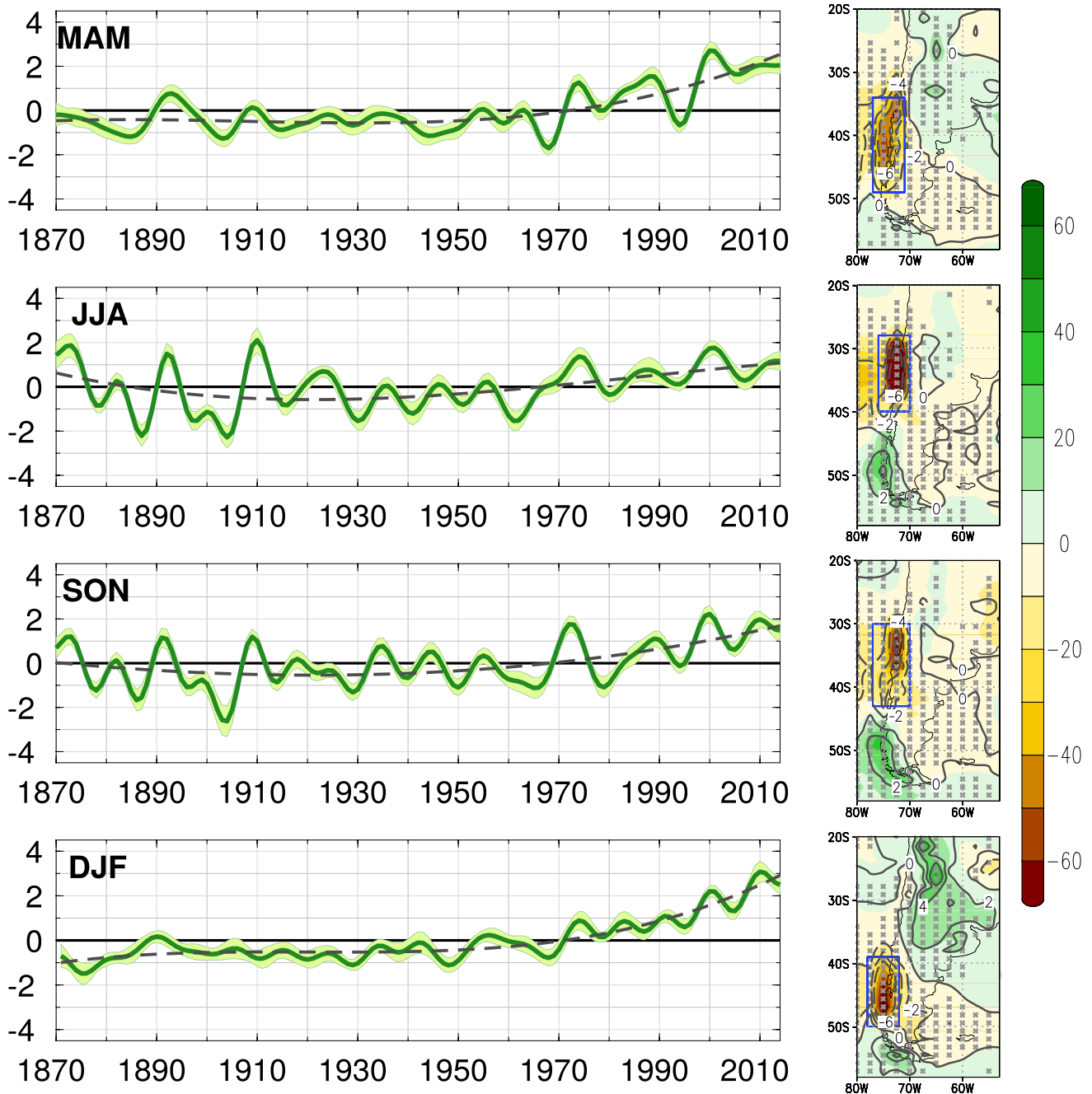


**Fig. 5** Main seasonal modes of precipitation low-frequency variability. Left panel: Standardized PC1s of the 8-year LPF seasonal precipitation anomalies over southern South America ( $58^{\circ}$ – $25^{\circ}$ S;  $80^{\circ}$ – $65^{\circ}$ W) from the amip-hist ensemble-mean. Explained variance of the PC1s: 59.1% in MAM, 75.7% in JJA, 67.0% in SON and 69.9% in DJF. Dotted lines indicate the 3th-degree polynomial fit and green shading the spread among members at the 95% confidence level. Right panel:

Regression patterns of the seasonal precipitation anomalies on the respective seasonal PC1 indices (shading; units are mm per standard deviation) and linear trend (contours; units are  $\text{mm decade}^{-1}$ ) over the entire simulated period, 1870–2014. Gray dots indicate where there is at least 80% agreement among members regarding the sign of the regression coefficient

and is strongly associated with the HC expansion. The rest of individual forcings generate no significant trends. In JJA and SON, GHGs alone induce a drying trend that respectively doubles and equals that caused by all forcing together and that is tightly linked to HC expansion.

In both seasons, ozone depletion also contributes to drying, but its impact is not associated with the HCE shift. In turn, aerosols and, to a lesser extent, natural forcings partially counteract the drying. Aerosols positive effect on precipitation is consistent with simultaneous



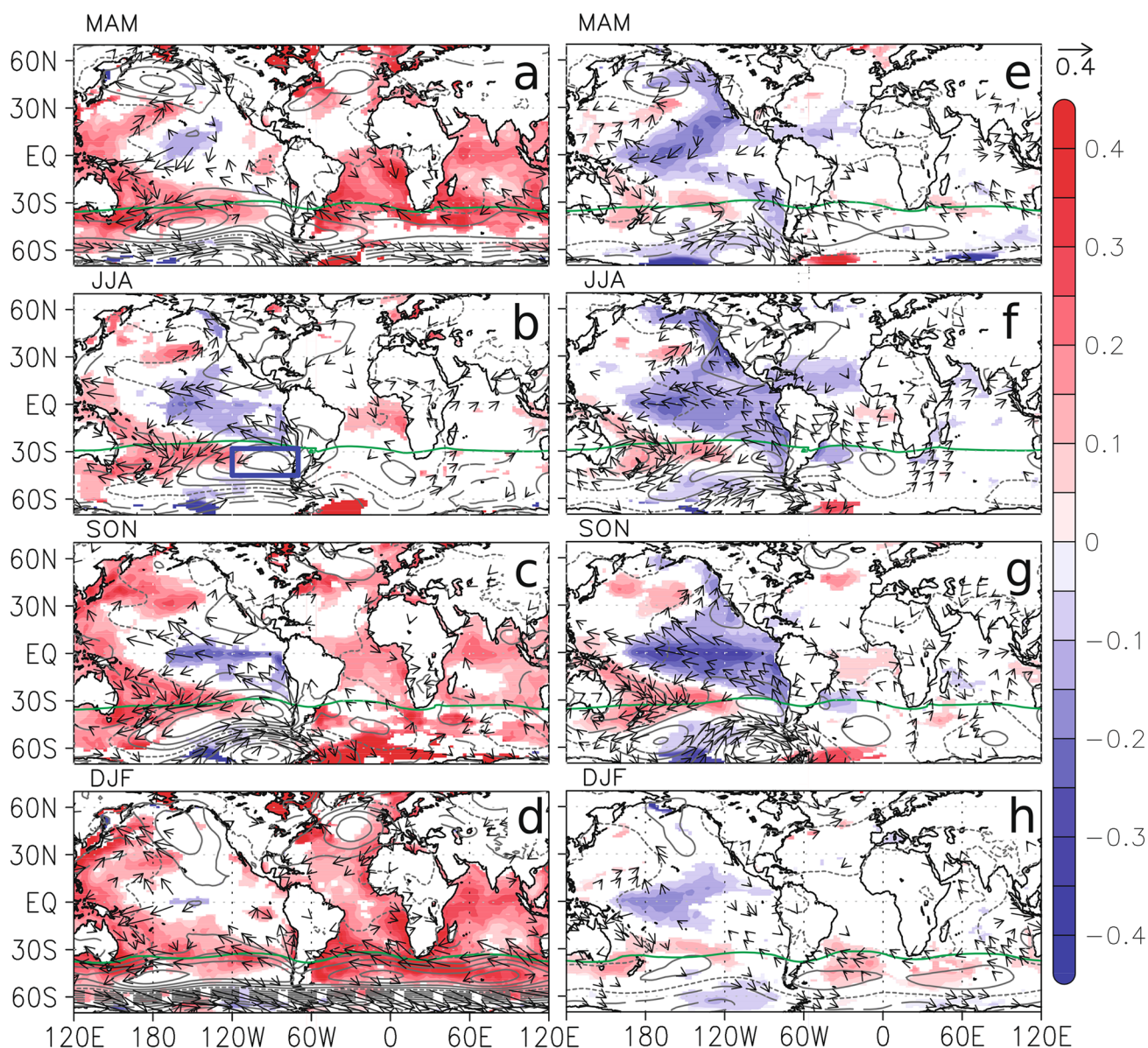


**Fig. 6** Seasonal regression patterns of the (a–d) non-detrended and (e–h) detrended indices of precipitation on the seasonal anomalies of SST (shaded; units are °C per standard deviation), surface wind (vectors;  $\text{m s}^{-1}$  per standard deviation) and SLP (contours in intervals of 0.2 hPa per standard deviation). Regression values of the SST and wind anomalies with lower than 80% statistical significance, accord-

ing to a random-phase test of Ebisuzaki, are masked. The green lines indicate the position of the climatological maximum of SLP. The patterns are computed using amip-hist ensemble-means. Blue box in **b** indicate a center of maximum SLP anomalies between 70°–120°W and 28°–45°S

HC contraction in these seasons. Nevertheless, the HCE index barely accounts for 23% and 18% of the total trend induced by aerosols respectively in JJA and SON. In DJF, the effect of GHGs and ozone depletion separately induce each around half of the trend displayed by the historical simulation, while the other forcings induce no significant trend. The HCE-coherent trend underestimates by 60% the drying attributed to GHGs but accounts for the entire trend induced by ozone depletion. The difference between

the ensemble-mean trend of the “sum” index of SWSA precipitation and the one from the historical simulation suggest that the effects of individual forcings are barely additive. Nevertheless, this difference is not statistically significant with high significance interval, due to the considerable uncertainty among individual members.



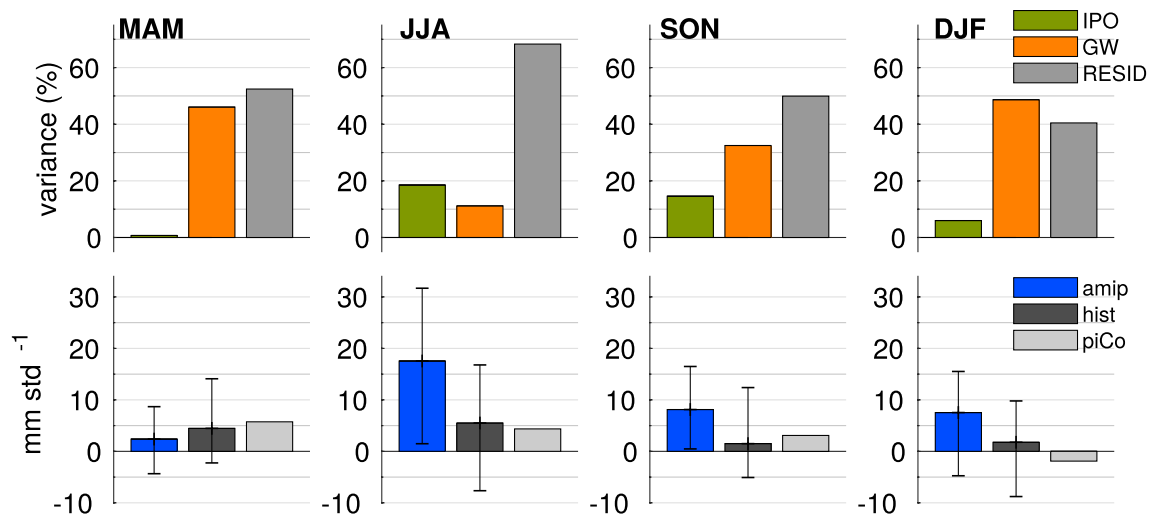


**Fig. 7** Decomposition of the SWSA precipitation variance in response to the IPO and GW indices, and simulated precipitation sensitivity to the IPO. Upper panel: Bar charts of the components of the total variance (in %) of the LPF indices of amip-hist ensemble-mean seasonal SWSA precipitation explained by the IPO (green) and GW (orange) indices and the residual (grey) resulting from a multi-linear

regression analysis. Bottom panel: Bar charts of the ensemble-mean regression coefficient between the SWSA precipitation seasonal anomalies and the standardized IPO index in amip-hist (blue), historical (black) and piControl (grey) simulations. Error bars indicate the total spread of the result obtained from individual members

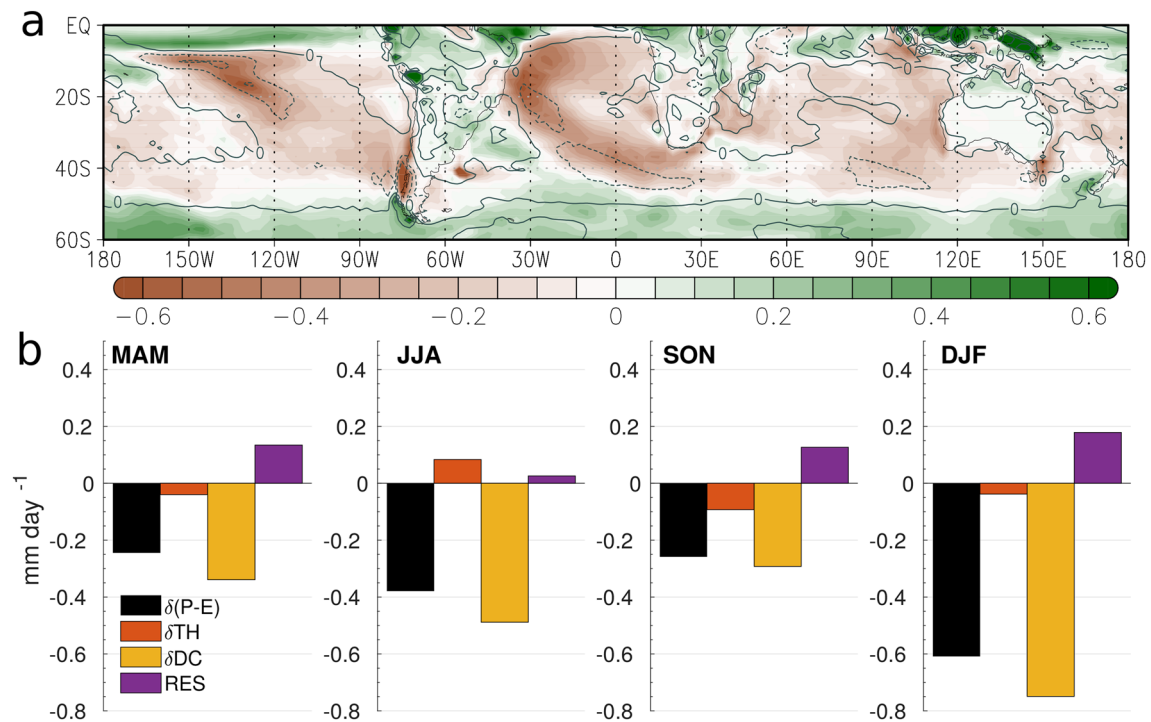


**Fig. 8** Decomposition of the net moisture budget change in SWSA. **a** Colors indicate the change in the annual-mean P-E averaged over 2005–2014 with respect to 1851–1910 in units of  $\text{mm day}^{-1}$ . Contours (in intervals of 0.1 from  $-0.2$  to  $0.2 \text{ mm day}^{-1}$  per standard deviation) indicate the regression of the annual P-E anomalies on the standardized annual HCE index over 1850–2014. **b** Bar charts of the

seasonal-mean change in the net moisture budget (black), the thermodynamic (orange) and dynamic (yellow) components and the residual (purple) averaged over the corresponding seasonal SWSA areas (see boxes in Fig. 5). All plots are based on the ensemble-mean of the historical simulations

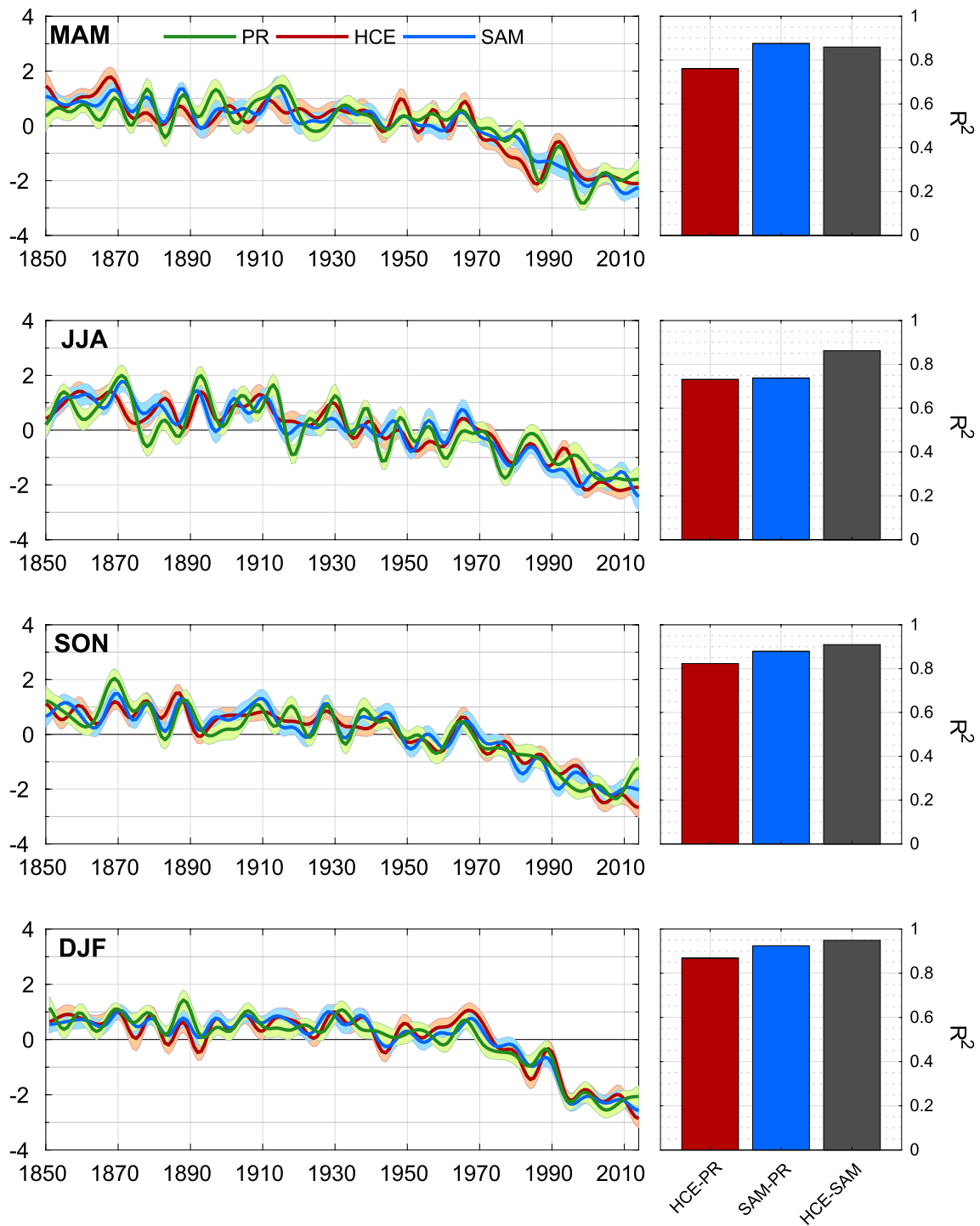


**Fig. 9** Left panel: Standardized seasonal indices of (green line) SWSA precipitation (PR), (red line) HCE and (blue line) -SAM from the historical ensemble mean (units are standard deviation). Shading

indicates the 95% confidence interval. Right panel:  $R^2$  values between the ensemble-mean (red bar) PR and HCE indices, (blue bar) PR and SAM indices and (gray bar) HCE and SAM indices

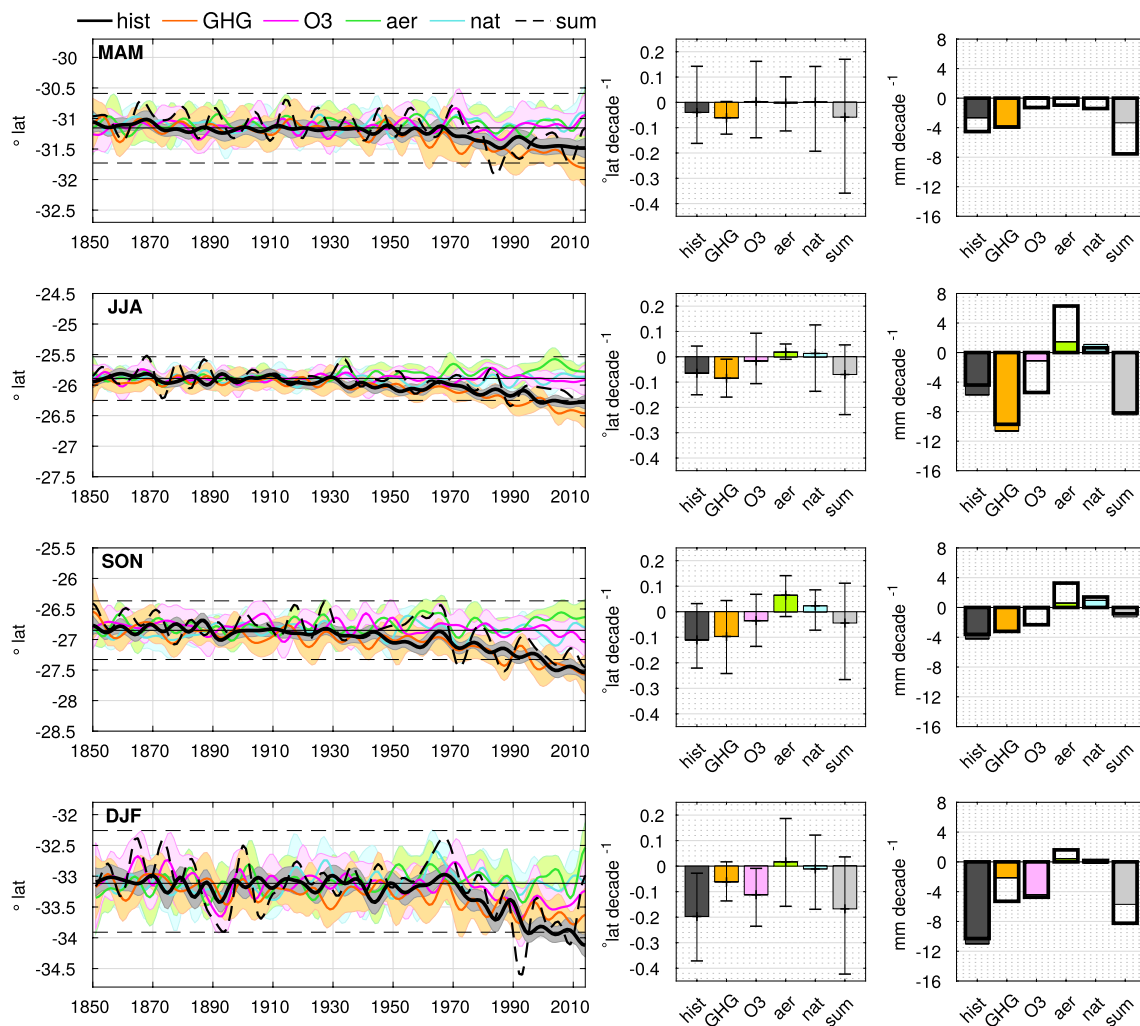


**Fig. 10** Left panel: Ensemble-mean HCE indices with 95% confidence interval of the (black) historical, (orange) hist-GHG, (pink) hist-O3, (green) hist-aer, (cyan) hist-nat simulations and the (dashed black) index obtained from the sum of the individual attribution run anomalies. Horizontal lines represent the (solid) climatology and (dashed) 90% dispersion of the piControl HCE anomalies. Middle panel: (color bars) Ensemble-mean HCE index linear trend over

1970–2014 and (error bars) spread from individual members. Right panel: (outlined black bars) Linear trend of the low-frequency index of ensemble-mean SWSA precipitation over 1970–2014 and (color bars) coherent trend with the ensemble-mean HCE index ( $\alpha \cdot \delta HCE$ ; where  $\alpha$  is the regression coefficient calibrated over the entire simulated period and  $\delta HCE$  the HCE trend over 1970–2014)

## 5 Discussion

### 5.1 The role of the IPO

Our results highlight the leading role of the SAM and the HCE on the recent SWSA long-term drying trend in response to anthropogenic forcings. This is in line with Boisier et al. (2018)’s finding showing that GHGs and the ozone depletion drive the SWSA drying trend over 1960–2016 in association with positive SAM anomalies. Nonetheless, Boisier et al. (2016) concludes that the forced drying trend at multidecadal scale can be substantially modulated by internal SST variability through the IPO. This previous work focuses on the 1979–2014 period and concludes, based on a linear

regression model, that approximately 40% of the SWSA drying trend is attributable to the concurrent pronounced negative trend in the IPO index (Fig. 3). This statement opposes our result on the decomposition of the decadal variance of SWSA precipitation, which reveals little influence of the IPO compared to external forcing (Fig. 7).

To shed light on this discrepancy, we focus on the IPO-coherent trend of precipitation over 1979–2014 using the ensemble-mean amip-hist precipitation (upper panel in Fig. 11). This trend exceeds the one attributable only to the internal variability of observed SST (i.e., the trend of ensemble-mean amip-hist precipitation minus the trend from the historical ensemble mean) in all seasons. This diagnostic evinces that a linear regression model can mislead the

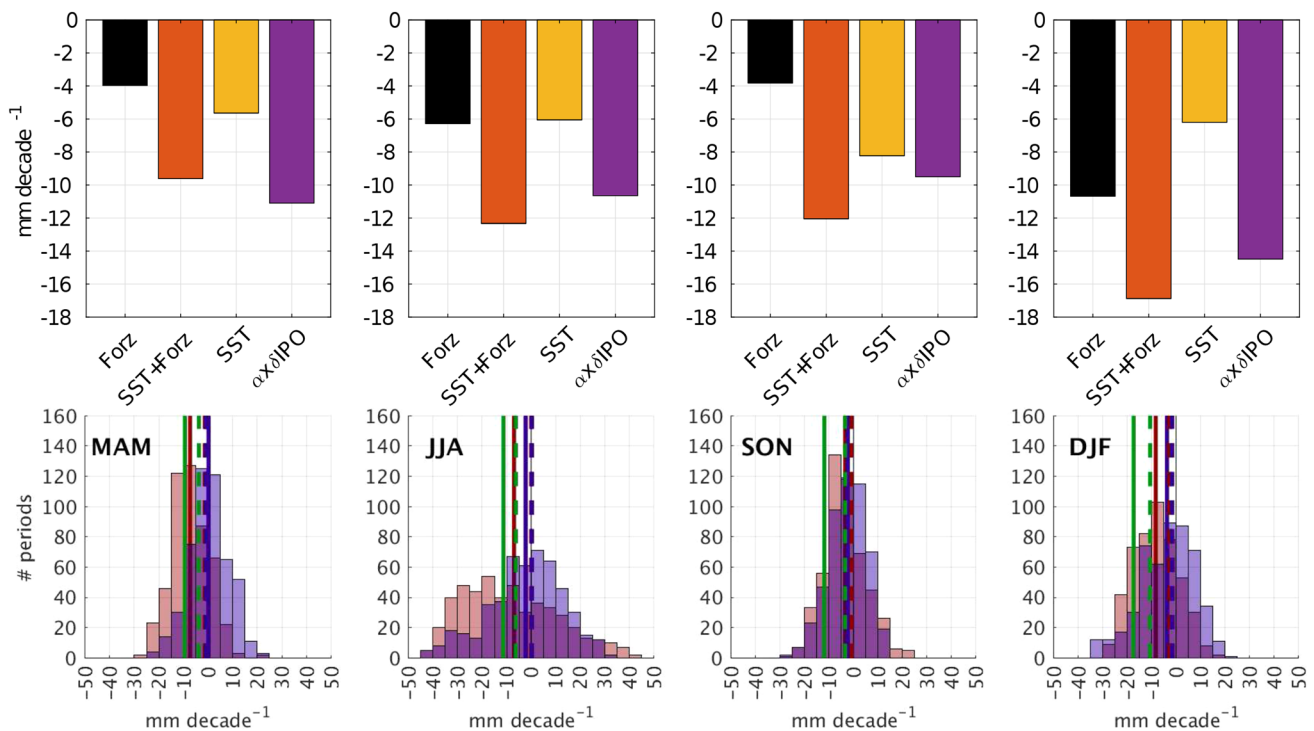


**Fig. 11** Upper panel: Trend of the seasonal SWSA precipitation over 1979–2014 induced by external forcing (Forz) (i.e., computed from the historical ensemble-mean), by observed SST and external forcing (SST + Forz) (i.e., computed from the amip-hist ensemble-mean), by only observed SST (i.e., computed as the trend from the amip-hist ensemble-mean minus the one from the historical ensemble-mean) and the trend associated with the trend of the IPO index with a linear regression over 1979–2014 ( $\alpha \cdot \delta IPO$ ). Bottom panel: PDFs of the seasonal SWSA precipitation linear trend (in  $\text{mm decade}^{-1}$ )

IPO signal on the SWSA precipitation with the trend associated with external forcing. On the other hand, the amip-hist ensemble-mean 1979–2014 drying trend notably exceeds the forced component represented by the ensemble mean of the historical coupled runs. This may suggest that the linear evolution of observed SST in 1979–2014, characterized by a steep negative IPO phase-shift, has a major contribution to the drought along with external forcing. Nevertheless, the amip-hist ensemble-mean precipitation trend may also represent an amplification of the forced drying by non-linear air-sea interactions and atmospheric processes rather than the signature of the specific IPO phase-shift.

To further assess whether the IPO phase shifts can directly induce decadal trends in the simulated SWSA precipitation, we perform PDFs of the precipitation trend over 1979–2014 and across all other possible 36-year periods since 1870 (bottom panel in Fig. 11). We use all the amip-hist members separately and represent the precipitation trend only in 36-year periods in which the IPO presents a phase shift and significant linear trend. 50 IPO trend values are obtained, equally distributed between positive

over 36-year periods since 1870 in the amip-hist individual members in which the IPO index shows positive (red bars) and negative (blue bars) phase shifts. The red/blue vertical solid lines indicate the trend averaged over all values corresponding to positive/negative IPO shifts. Vertical green lines indicate the 1979–2014 trends in the ensemble-mean amip-hist. Vertical red, blue and green dashed lines represent equivalent trends to the respective colored solid lines but corresponding to the historical simulations

and negative shifts ranging between  $\pm 0.09 \text{ }^\circ\text{C}$  per decade centered on respective means of  $0.17 \text{ }^\circ\text{C}$  and  $-0.16 \text{ }^\circ\text{C}$  per decade. Then the precipitation trend values are classified according to whether the shift is from a negative to a positive IPO phase (red bars) or vice versa (blue bars). According to a two-sample t-test, the null hypothesis that the red and the blue PDFs show normal distributions with equal means and variances cannot be rejected, considering low confidence intervals ( $p > 0.92$ ) in all seasons. Their means, represented by the red and blue solid vertical lines, show weak changes compared to the ensemble-mean trend over 1979–2014 (green solid lines; corresponding to an IPO shift of  $-0.21 \text{ }^\circ\text{C}$  per decade). But they are negative in all cases, except in MAM where the blue line indicates an almost null positive trend ( $0.2 \text{ mm per decade}$ ). Therefore, these results suggest no significant relationship between the linear trend of the simulated precipitation and the sign of the IPO phase shifts over 36-year periods.

This conclusion is supported by similar PDFs performed using the 32 historical members (not shown). The resulting PDFs are not significantly different between each other and

to the previous ones from the amip-hist simulations, according to a two-sample t-test. In addition, the resulting mean trends (red and blue dashed vertical lines in Fig. 11) are weaker than the drying represented by the historical ensemble mean over 1979–2014 in all seasons (green dashed lines) but negative in most cases, consistently with the amip-hist simulations, or positive but almost zero in JJA.

In contrast, the same analysis applied to trends over 20-year or shorter periods across the amip-hist simulations reveals a break up between the red and blue PDFs (not shown). They show prevailing positive (negative) rainfall trends concurrent with positive (negative) IPO phase shifts. This means that the amip-hist simulations can reproduce SWSA precipitation trends in response to IPO phase shifts at intradecadal-to-decadal time scales, in agreement with other works based on instrumental data (Masiokas et al. 2010). However, at multidecadal-to-longer timescales, such as the 36-year-long negative IPO trend observed since the 1979, the simulated effect of the IPO over the last century and a half vanishes and becomes insignificant compared to the leading role of external forcings.

In summary, our results show that the IPO explains little variance of SWSA precipitation multidecadal variability over the last century and a half, compared to external forcings. However, during 1979–2014 the simulated SWSA drying trend attributable only to internal variability of observed SST accounts for a large part of the total trend (Fig. 11). Therefore, we can conclude that the IPO is not a leading cause of long-term variability of SWSA precipitation, but it can contribute to amplified forced drying trends.

It has to be considered that the methodology used in this work is conditioned by the IPSL-CM6A-LR model biases in the atmospheric circulation. Therefore, the IPO influence on SWSA precipitation long-term variability should be assessed in the multi-model framework of CMIP6 to strengthen this conclusion.

## 5.2 The simulated HC expansion

Regarding the simulated seasonality in HCE, model trend values are comparable with those from observations, with simulations reproducing a poleward expansion over recent decades. In agreement with Hu et al. (2011, 2018) and model-based studies (Staten et al. 2012; Hu et al. 2013; Grise et al. 2018), the HCE expansion shows strong seasonality, being larger in austral summer (DJF) than in other seasons. Nevertheless, it is difficult to constrain a precise widening rate of the HCE expansion due to the large spread among the trends from reanalyses and the ensemble simulations. Regarding the wide range of trend values resulting from the simulated ensemble members, it can be inferred that some part of the large uncertainty is attributable to internal variability. In turn, observed and simulated trends

are comparable when the internal variability is considered, suggesting that a large part of the observed HCE expansion is accounted for by internal atmospheric variability (Grise et al. 2018). On the other hand, there is also large discrepancy in the HCE expansion rates derived from the different reanalyses. Apart from differences associated with distinct assimilation methods and model biases, this large discrepancy has been attributed, in part, to shortcomings regarding the conservation of mass in the meridional mean circulation (Davis and Davis 2018), especially in old generation reanalyses (Grise et al. 2019).

## 5.3 HCE and SAM co-linearity

Our results show strong co-linearity between the SAM, HCE and SWSA precipitation, evidencing that both modes induce changes on precipitation in the same direction. Furthermore, the simulated SAM strengthening and the HCE expansion are attributed to the same external forcings. This suggests a connection between circulation changes in tropical and high latitudes through a link of both variability modes under the effect of external forcing, in agreement with previous works (Thompson and Wallace 2000; Previdi and Liepert 2007). GCMs simulate an anomalous rise of the extratropical troposphere in association with the SAM strengthening (Previdi and Liepert 2007) and the expansion of the HCE (Lu et al. 2007) in future projections that consider strong external forcing effects. These anomalies are related to the increase of atmospheric static stability, which in turn is associated with a poleward expansion of the tropospheric baroclinicity. Subsequently, there is a shift in the same direction of the hemispheric circulation such as the westerly jets, which involves changes in both the SAM (Thompson et al. 2000) and the HCE (Staten et al. 2019), and in the mid-latitude storm-tracks modulating the SWSA precipitation. Nevertheless, the factors that control the extratropical atmospheric static instability are still unknown and, by extension, the mechanisms that explain the link between changes in the SAM and the HCE.

## 5.4 The role of anthropogenic forcing

Our results show that anthropogenic forcings have largely induced the recent SWSA drying through dynamical changes associated with the HCE and SAM. GHGs play the leading role on the HC expansion and the subsequent SWSA drying trend all year round except in DJF. In this season, the effect of GHGs is combined with the ozone depletion, which is the dominant factor. Although not shown in this paper, the leading effects of GHGs and ozone depletion are found to be similar on the HCE and the SAM. We also find that the effect of anthropogenic aerosols can offset the simulated HC expansion and the SWSA drying trend over 1970–2014. This



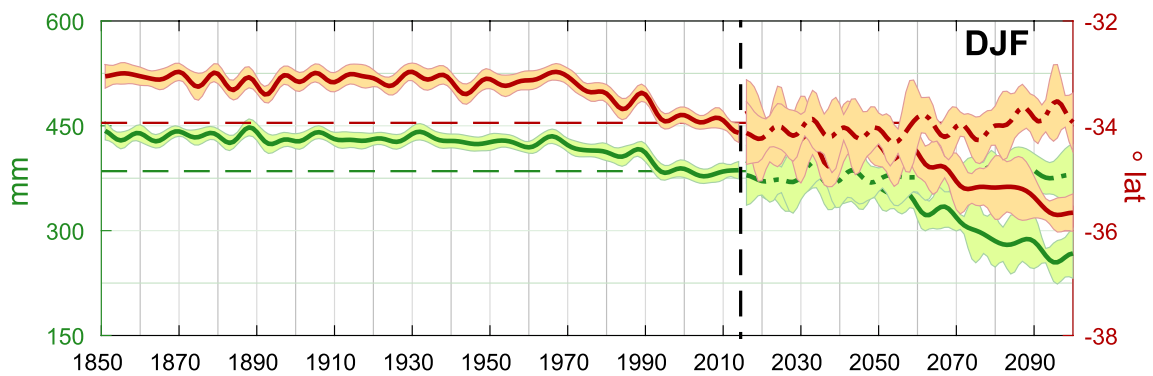
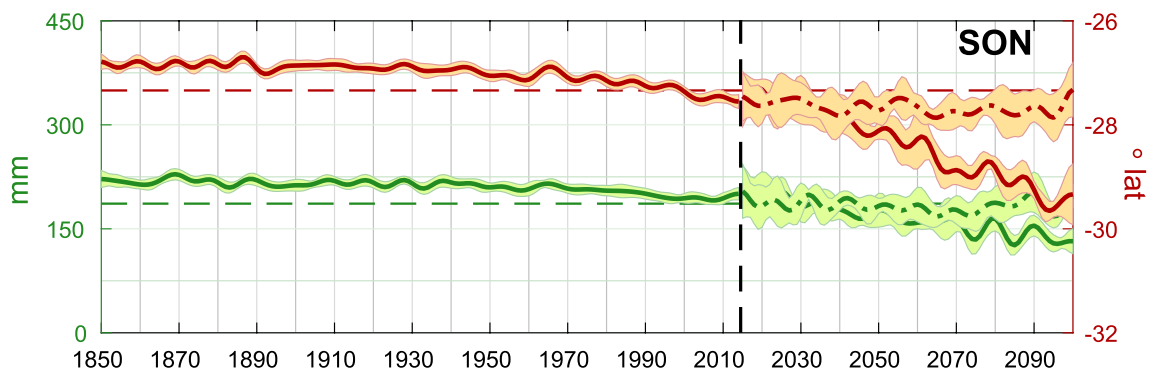
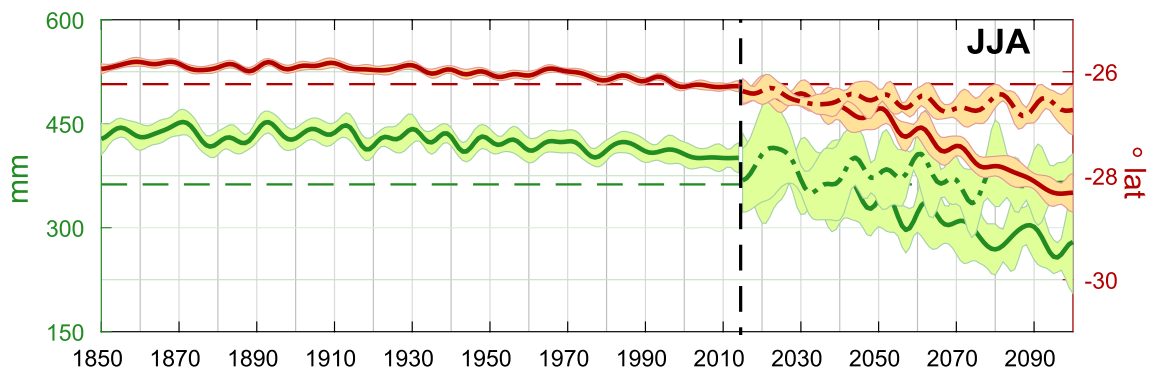
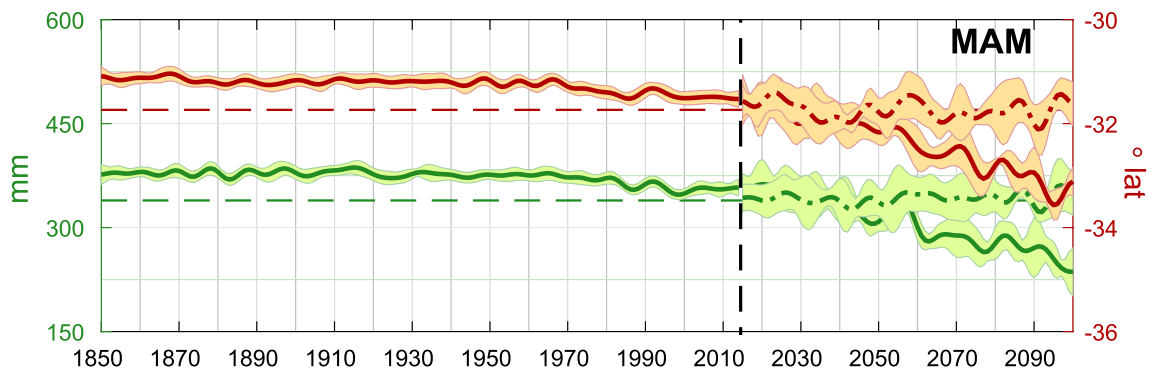


**Fig. 12** Seasonal indices of (green) SWSA precipitation and (red) HCE, computed from the ensemble mean of the historical simulations in 1850–2014 and in 2015–2100 of (solid line) the ssp585 and the (dashed line) the ssp126 future projections. Shading indicates the 95% confidence interval. Horizontal dashed lines indicate the lower threshold of the dispersion of the piControl (red) HCE and (green) SWSA precipitation anomalies with 90% confidence interval

is most likely related to the counteracting effect of aerosols on the global warming induced by GHGs (Andreae et al. 2005). However, the HC contraction barely explains a fraction of the forced rainfall increase, which is largest in JJA (Fig. 10) coincident with positive thermodynamics of the P–E imbalance (Fig. 8). This suggests that aerosols may induce precipitation changes in SWSA through thermodynamical processes. Nevertheless, aerosols effects are highly uncertain and poorly constrained by climate models (Andreae et al. 2005; Boucher et al. 2013; Carslaw et al. 2013; Oudar et al. 2018), suggesting that further investigation should be done to shed light on this concern.

### 5.5 Projected of HCE and SWSA precipitation

Aerosol emissions are likely to decrease in the future intensifying the GHGs effect (Andreae et al. 2005) concurrently with the stratospheric ozone recovery (Eyring et al. 2010). Consequently, an acceleration of HC expansion associated with aerosol depletion during JJA and SON could be expected in the coming years. At the same time, a slowdown of HC would occur in DJF with ozone recovery. However, no solid assumptions on the HCE future changes and the subsequent impacts on SWSA precipitation can be made without taking into account the evolution of GHG emissions. To address this concern, we analyze the ssp585 and the ssp126 future projections, which incorporate the aforementioned future evolution of the aerosols and stratospheric ozone under business-as-usual and mitigation scenarios of GHG emissions simultaneously (Lurton et al. 2020). The resulting ensemble-mean indices of HCE and SWSA precipitation are represented in Fig. 12, following those of the historical simulations. The ssp585 projection shows a sustained poleward expansion of the HCE in response to the substantial radiative forcing increase until the end of the current century. This result is consistent with previous work based on different GCMs (Grise et al. 2018; Staten et al. 2018). A SWSA drying follows the HC expansion in all seasons. The projected drying exceeds the threshold of extreme drought due to internal variability by the 2040s in MAM and JJA, the 2030s in SON. In DJF, the drying is shown to be extreme since the 2000s, according to the historical simulation. The yearly precipitation over 2091–2100 is projected to be 37% lower with respect to 1851–1910 along with an annual-mean HCE poleward shift of 2.4°lat. In turn, ssp126 experiment projects a 13% loss of yearly precipitation and an

annual-mean HC poleward expansion of 0.7°lat. This mitigation scenario represents a stabilization of the HC expansion and the SWSA drying close to the threshold of extreme rates in all seasons rather than a recovery.

Under the ssp585 scenario, an intense moisture deficit is also projected by the end of the twenty-first century in other subtropical regions, apart from SWSA (Fig. 13). Coastal areas in southern Angola and Namibia, south of South Africa, western and southeastern Australia also show negative P–E change associated with the HCE evolution. The historical simulation, in contrast, does not show such strong link in these regions (Fig. 8a). This suggests that the HC expansion could become an essential modulator of precipitation in these mostly dry regions as in SWSA in a future with high GHGs emissions. To further understand and attribute the future evolution of precipitation in these regions, the contribution of the HC expansion against thermodynamical direct effects and the relative role of external forcings with respect to internal long-term variability should be addressed more thoroughly.

## 6 Conclusions

The IPSL-CM6A-LR model simulates an emerging long-term drying trend in SWSA roughly since the early 1980s in response to the observed SST and external forcings, consistent with observations and other GCMs (e.g., Vera and Díaz 2015; Boisier et al. 2018). A modulating effect of the internal SST variability on the simulated SWSA drying over 1979–2014 is detected, related to the IPO as suggested by previous work (Boisier et al. 2016). However, the simulated impact of the IPO on the overall decadal variability of SWSA precipitation across the last century and a half is found to be weak and secondary compared to the effect of external forcings.

The external forcing modulates the simulated SWSA precipitation indirectly through dynamic changes, prevailing over direct thermodynamic effects. Specifically, this work relates the simulated drought in SWSA with a concurrent strengthening of the SAM and expansion of the HC, which occur in response to external forcings. Simulated forced changes in these two variability modes act on SWSA precipitation in the same direction and respond to the same components of external forcings. Both modes react more strongly to external forcing in DJF than in other seasons principally in response to the stratospheric ozone depletion and, in second place, to the GHGs, in agreement with previous studies (e.g., Polvani et al. 2011; Kim et al. 2017; Jebri et al. 2020). In the rest of the seasons, the ozone depletion effect is weaker and the GHG forcing prevails. Future projections suggest that the GHG effect determines the HCE,

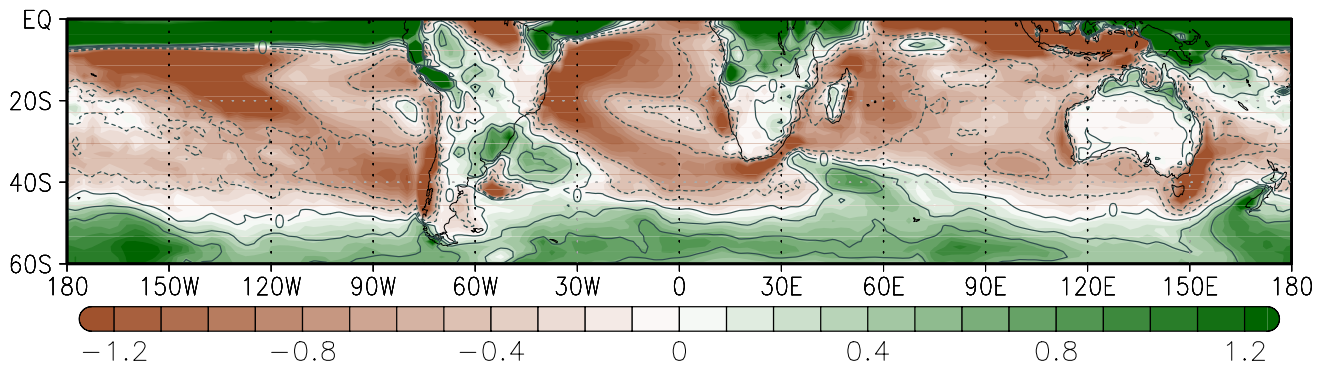


**Fig. 13** Projected change of the net moisture budget in the Southern Hemisphere. Colors indicate the change in the annual-mean P-E (units are  $\text{mm day}^{-1}$ ) averaged over 2091–2100 with respect to 2005–2014, based on ensemble-mean ssp585 and historical outputs, respec-

tively. Contours (in intervals of 0.1 from  $-0.2$  to  $0.2 \text{ mm day}^{-1}$  per standard deviation) indicate the regression of annual P-E anomalies on the standardized annual HCE index over 2015–2100

and consequently, the long-term variability in SWSA precipitation throughout the twenty-first century.

**Acknowledgements** The authors thank editor Dr. Corti and the two anonymous reviewers for their fundamental duty in the publishing process of this paper and their helpful comments. This work was undertaken in the framework of the THEMES project under the BNP-Paribas Foundation grant and the IPSL Climate Graduate School EUR. The CMIP6 project at IPSL used the HPC resources of TGCC under the allocations 2016-A0030107732, 2017-R0040110492 and 2018-R0040110492 (project gencmip6) provided by GENCI (Grand Equipement National de Calcul Intensif). This study benefited from the ESPRI (Ensemble de Services Pour la Recherche l'IPSL) computing and data centre (<https://mesocentre.ipsl.fr>) which is supported by CNRS, Sorbonne Université, Ecole Polytechnique and CNES and through national and international grants. Special thanks to Juan Rivera for providing us with observational precipitation data from rain gauges and his helpful comments on the model validation.

## References

- Alexander MA, Bladé I, Newman M, Lanzante JR, Lau NC, Scott JD (2002) The atmospheric bridge: the influence of ENSO teleconnections on air–sea interaction over the global oceans. *J Climate* 15(16):2205–2231
- Allan R, Ansell T (2006) A new globally complete monthly historical gridded mean sea level pressure dataset (HADSLP2): 1850–2004. *J Climate* 19(22):5816–5842
- Allen RJ, Kovilakam M (2017) The role of natural climate variability in recent tropical expansion. *J Climate* 30(16):6329–6350
- Amaya DJ, Siler N, Xie SP, Miller AJ (2018) The interplay of internal and forced modes of Hadley cell expansion: lessons from the global warming hiatus. *Climate Dyn* 51(1–2):305–319
- Andreae MO, Jones CD, Cox PM (2005) Strong present-day aerosol cooling implies a hot future. *Nature* 435(7046):1187–1190
- Aumont O, Éthé C, Tagliabue A, Bopp L, Gehlen M (2015) Pisces-v2: an ocean biogeochemical model for carbon and ecosystem studies. *Geosci Model Dev* 8(8):2465–2513
- Barrett BS, Hameed S (2017) Seasonal variability in precipitation in central and southern Chile: modulation by the south Pacific high. *J Climate* 30(1):55–69
- Boisier JP, Rondanelli R, Garreaud RD, Muñoz F (2016) Anthropogenic and natural contributions to the southeast Pacific precipitation decline and recent megadrought in central Chile. *Geophys Res Lett* 43(1):413–421
- Boisier JP, Alvarez-Garretón C, Cordero RR, Damiani A, Gallardo L, Garreaud RD, Lambert F, Ramallo C, Rojas M, Rondanelli R (2018) Anthropogenic drying in central-southern Chile evidenced by long-term observations and climate model simulations. *Elementa* 1000:6. <https://doi.org/10.1525/elementa.328>
- Boucher O, Randall D, Artaxo P, Bretherton C, Feingold G, Forster P, Kerminen VM, Kondo Y, Liao H, Lohmann U et al (2013) Clouds and aerosols. In: *Climate change 2013: the physical science basis. Contribution of Working Group I to the Fifth Assessment Report of the Intergovernmental Panel on Climate Change*, Cambridge University Press, pp 571–657
- Boucher O, Servonnat J, Albright AL, Aumont O, Balkanski Y, Bastrikov V, Bekki S, Bonnet R, Bony S, Bopp L et al (2020) Presentation and evaluation of the IPSL-CM6A-LR climate model. *J Adv Model Earth Syst* 12(7):e2019MS002010
- Brubaker KL, Entekhabi D, Eagleson P (1993) Estimation of continental precipitation recycling. *J Climate* 6(6):1077–1089
- Butterworth S (1930) On the theory of filter amplifiers. *Wirel Eng* 7(6):536–541
- Carlsaw K, Lee L, Reddington C, Pringle K, Rap A, Forster P, Mann G, Spracklen D, Woodhouse M, Regayre L et al (2013) Large contribution of natural aerosols to uncertainty in indirect forcing. *Nature* 503(7474):67–71
- Carvalho LM, Jones C, Ambrizzi T (2005) Opposite phases of the Antarctic oscillation and relationships with intraseasonal to interannual activity in the tropics during the austral summer. *J Climate* 18(5):702–718
- Checa-Garcia R, Hegglin MI, Kinnison D, Plummer DA, Shine KP (2018) Historical tropospheric and stratospheric ozone radiative forcing using the CMIP6 database. *Geophys Res Lett* 45(7):3264–3273
- Compo GP, Whitaker JS, Sardeshmukh PD, Matsui N, Allan RJ, Yin X, Gleason BE, Vose RS, Rutledge G, Bessemoulin P et al (2011) The twentieth century reanalysis project. *Q J R Meteorol Soc* 137(654):1–28
- CR2 (2015) Report to the nation. the 2010–2015 mega-drought: a lesson for the future. Center for Climate and Resilience Research (CR2) 28
- Davis N, Davis SM (2018) Reconciling Hadley cell expansion trend estimates in reanalyses. *Geophys Res Lett* 45(20):11–439

- Dee D, Balmaseda M, Balsamo G, Engelen R, Simmons A, Thépaut JN (2014) Toward a consistent reanalysis of the climate system. *Bull Am Meteorol Soc* 95(8):1235–1248
- d'Orgeval T, Polcher J, Rosnay Pd (2008) Sensitivity of the west African hydrological cycle in orchidee to infiltration processes. *Hydrol Earth Syst Sci* 12(6):1387–1401
- Ebisuzaki W (1997) A method to estimate the statistical significance of a correlation when the data are serially correlated. *J Climate* 10(9):2147–2153
- Eyring V, Cionni I, Lamarque JF, Akiyoshi H, Bodeker G, Charlton-Perez A, Frith S, Gettelman A, Kinnison D, Nakamura T et al (2010) Sensitivity of 21st century stratospheric ozone to greenhouse gas scenarios. *Geophys Res Lett* 37(16):L16807
- Eyring V, Bony S, Meehl GA, Senior CA, Stevens B, Stouffer RJ, Taylor KE (2016) Overview of the coupled model intercomparison project phase 6 (cmip6) experimental design and organization. *Geosci Model Dev (Online)* 9:LLNL-JRNL-736881
- Falvey M, Garreaud R (2007) Wintertime precipitation episodes in central chile: Associated meteorological conditions and orographic influences. *J Hydrometeorol* 8(2):171–193
- Fogt RL, Marshall GJ (2020) The southern annular mode: variability, trends, and climate impacts across the southern hemisphere. *Wiley Interdiscip Rev Climate Change* 11(4):e652
- Fogt RL, Jones JM, Renwick J (2012) Seasonal zonal asymmetries in the southern annular mode and their impact on regional temperature anomalies. *J Climate* 25(18):6253–6270
- Folland C, Parker D, Colman A, Washington R (1999) Large scale modes of ocean surface temperature since the late nineteenth century. In: *Beyond El Niño*. Springer, Berlin, pp 73–102
- Garreaud R, Lope P, Minvielle M, Rojas M (2013) Large-scale control on the patagonian climate. *J Climate* 26(1):215–230
- Garreaud RD, Vuille M, Compagnucci R, Marengo J (2009) Present-day south american climate. *Palaeogeogr Palaeoclimatol Palaeoecol* 281(3–4):180–195
- Garreaud RD, Alvarez-Garretón C, Barichivich J, Boisier JP, Christie D, Galleguillos M, LeQuesne C, McPhee J, Zambrano-Bigiarini M (2017) The 2010–2015 megadrought in central chile: impacts on regional hydroclimate and vegetation. *Hydrol Earth Syst Sci* 21(12):6307–6327
- Garreaud RD, Boisier JP, Rondanelli R, Montecinos A, Sepúlveda HH, Veloso-Aguila D (2020) The central chile mega drought (2010–2018): a climate dynamics perspective. *Int J Climatol* 40(1):421–439
- Gillett NP, Thompson DW (2003) Simulation of recent southern hemisphere climate change. *Science* 302(5643):273–275
- Gillett NP, Shiogama H, Funke B, Hegerl G, Knutti R, Matthes K, Santer BD, Stone D, Tebaldi C (2016) The detection and attribution model intercomparison project (DAMIP v1.0) contribution to CMIP6. *Geosci Model Dev* 9(10):3685–3697
- Gong D, Wang S (1999) Definition of Antarctic oscillation index. *Geophys Res Lett* 26(4):459–462
- Grise KM, Davis SM, Staten PW, Adam O (2018) Regional and seasonal characteristics of the recent expansion of the tropics. *J Climate* 31(17):6839–6856
- Grise KM, Davis SM, Simpson IR, Waugh DW, Fu Q, Allen RJ, Rosenlof KH, Ummenhofer CC, Karnauskas KB, Maycock AC et al (2019) Recent tropical expansion: natural variability or forced response? *J Climate* 32(5):1551–1571
- Helpd IM, Soden BJ (2006) Robust responses of the hydrological cycle to global warming. *J Climate* 19(21):5686–5699
- Henley BJ, Gergis J, Karoly DJ, Power S, Kennedy J, Folland CK (2015) A triple index for the interdecadal pacific oscillation. *Climate Dyn* 45(11–12):3077–3090
- Hoesly RM, Smith SJ, Feng L, Klimont Z, Janssens-Maenhout G, Pitkanen T, Seibert JJ, Vu L, Andres RJ, Bolt RM et al (2018) Historical (1750–2014) anthropogenic emissions of reactive gases and aerosols from the community emissions data system (ceds). *Geosci Model Dev* 11(1):369–408
- Hourdin F, Rio C, Grandpeix JY, Madeleine JB, Cheruy F, Rochetin N, Jam A, Musat I, Idelkadi A, Fairhead L et al (2020) LMDZ6A: the atmospheric component of the IPSL climate model with improved and better tuned physics. *J Adv Model Earth Syst* 12(7):e2019MS001892
- Hu Y, Zhou C, Liu J (2011) Observational evidence for poleward expansion of the hadley circulation. *Adv Atmos Sci* 28(1):33–44
- Hu Y, Tao L, Liu J (2013) Poleward expansion of the hadley circulation in cmip5 simulations. *Adv Atmos Sci* 30(3):790–795
- Hu Y, Huang H, Zhou C (2018) Widening and weakening of the hadley circulation under global warming. *Sci Bull* 63(10):640–644
- Jebri B, Khodri M, Echevin V, Gastineau G, Thiria S, Vialard J, Lebas N (2020) Contributions of internal variability and external forcing to the recent trends in the southeastern pacific and peru-chile upwelling system. *J Climate* 33(24):10555–10578
- Kalnay E, Kanamitsu M, Kistler R, Collins W, Deaven D, Gandin L, Iredell M, Saha S, White G, Woollen J et al (1996) The NCEP/NCAR 40-year reanalysis project. *Bull Am Meteorol Soc* 77(3):437–472
- Kim YH, Min SK, Son SW, Choi J (2017) Attribution of the local hadley cell widening in the southern hemisphere. *Geophys Res Lett* 44(2):1015–1024
- Lu J, Vecchi GA, Reichler T (2007) Expansion of the Hadley cell under global warming. *Geophys Res Lett* 34(6):L06805
- Lurton T, Balkanski Y, Bastrikov V, Bekki S, Bopp L, Braconnot P, Brockmann P, Cadule P, Contoux C, Cozic A et al (2020) Implementation of the cmip6 forcing data in the IPSL-CM6A-LR model. *J Adv Model Earth Syst* 12(4):e2019MS001940
- Mantua NJ, Hare SR, Zhang Y, Wallace JM, Francis RC (1997) A pacific interdecadal climate oscillation with impacts on salmon production. *Bull Am Meteorol Soc* 78(6):1069–1080
- Masiokas M, Cara L, Villalba R, Pitte P, Luckman B, Toum E, Christie D, Le Quesne C, Mauget S (2019) Streamflow variations across the andes (18–55 s) during the instrumental era. *Sci Rep* 9(1):1–13
- Masiokas MH, Villalba R, Luckman BH, Mauget S (2010) Intra-to multidecadal variations of snowpack and streamflow records in the andes of chile and argentina between 30 and 37 s. *J Hydrometeorol* 11(3):822–831
- Matthes K, Funke B, Anderson M, Barnard L, Beer J, Charbonneau P, Clilverd M, Dudok de Wit T, Haberreiter M, Hendry A, et al. (2017) Solar forcing for cmip6 (v3. 2). *Geoscientific Model Development* 10(6):2247–2302
- McPhaden MJ, Zebiak SE, Glantz MH (2006) ENSO as an integrating concept in earth science. *Science* 314(5806):1740–1745
- Meehl GA, Hu A (2006) Megadroughts in the indian monsoon region and southwest North America and a mechanism for associated multidecadal Pacific sea surface temperature anomalies. *J Climate* 19(9):1605–1623
- Meehl GA, Hu A, Santer BD (2009) The mid-1970s climate shift in the pacific and the relative roles of forced versus inherent decadal variability. *J Climate* 22(3):780–792
- Meinshausen M, Vogel E, Nauels A, Lorbacher K, Meinshausen N, Etheridge DM, Fraser PJ, Montzka SA, Rayner PJ, Trudinger CM et al (2017) Historical greenhouse gas concentrations for climate modelling (CMIP6). *Geosci Model Dev* 10:2057–2116
- Meza FJ, Wilks DS, Gurovich L, Bambach N (2012) Impacts of climate change on irrigated agriculture in the Maipo Basin, Chile: reliability of water rights and changes in the demand for irrigation. *J Water Resour Plan Manag* 138(5):421–430
- Mohino E, Keenlyside N, Pohlmann H (2016) Decadal prediction of Sahel rainfall: where does the skill (or lack thereof) come from? *Climate Dyn* 47(11):3593–3612



- Montecinos A, Aceituno P (2003) Seasonality of the ENSO-related rainfall variability in central Chile and associated circulation anomalies. *Journal of climate* 16(2):281–296
- Newman M, Alexander MA, Ault TR, Cobb KM, Deser C, Di Lorenzo E, Mantua NJ, Miller AJ, Minobe S, Nakamura H et al (2016) The Pacific decadal oscillation, revisited. *J Climate* 29(12):4399–4427
- Nguyen H, Evans A, Lucas C, Smith I, Timbal B (2013) The Hadley circulation in reanalyses: climatology, variability, and change. *J Climate* 26(10):3357–3376
- Norero A, Bonilla CA (1999) Las sequías en Chile: Causas, consecuencias y mitigación. Pontificia Universidad Católica de Chile Facultad de agronomía e ingeniería forestal Santiago de Chile, p 128
- O'Neill BC, Tebaldi C, Vuuren DPv, Eyring V, Friedlingstein P, Hurtt G, Knutti R, Kriegler E, Lamarque JF, Lowe J et al (2016) The scenario model intercomparison project (ScenarioMIP) for CMIP6. *Geosci Model Dev* 9(9):3461–3482
- Oudar T, Kushner PJ, Fyfe JC, Sigmund M (2018) No impact of anthropogenic aerosols on early 21st century global temperature trends in a large initial-condition ensemble. *Geophys Res Lett* 45(17):9245–9252
- Pabón-Caicedo JD, Arias PA, Carril AF, Espinoza JC, Goubanova K, Lavado W, Masiokas M, Solman SA, Villalba R (2020) Observed and projected hydroclimate changes in the Andes. *Front Earth Sci* 8:61
- Polvi P, Hersbach H, Dee DP, Berrisford P, Simmons AJ, Vitart F, Lalouaux P, Tan DG, Peubey C, Thépaut JN et al (2016) ERA-20c: an atmospheric reanalysis of the twentieth century. *J Climate* 29(11):4083–4097
- Polvani LM, Waugh DW, Correa GJ, Son SW (2011) Stratospheric ozone depletion: The main driver of twentieth-century atmospheric circulation changes in the southern hemisphere. *J Climate* 24(3):795–812
- Previdi M, Liepert BG (2007) Annular modes and Hadley cell expansion under global warming. *Geophys Res Lett* 34(22):105
- Quintana J, Aceituno P (2012) Changes in the rainfall regime along the extratropical west coast of South America (Chile): 30–43°S. *Atmósfera* 25(1):1–22
- Rayner N, Parker DE, Horton E, Folland CK, Alexander LV, Rowell D, Kent E, Kaplan A (2003) Global analyses of sea surface temperature, sea ice, and night marine air temperature since the late nineteenth century. *J Geophys Res Atmos* 108(D14):4407
- Rivera JA, Arnould G (2020) Evaluation of the ability of CMIP6 models to simulate precipitation over southwestern South America: climatic features and long-term trends (1901–2014). *Atmos Res* 241:104953
- Rosegrant MW, Ringler C, McKinney DC, Cai X, Keller A, Donoso G (2000) Integrated economic-hydrologic water modeling at the basin scale: the MAIPO river basin. *Agric Econ* 24(1):33–46
- Rousset C, Vancoppenolle M, Madec G, Fichet T, Flavoni S, Barthélemy A, Benschila R, Chanut J, Lévy C, Masson S et al (2015) The Louvain-la-Neuve sea ice model LIM3.6: global and regional capabilities. *Geosci Model Dev* 8(10):2991–3005
- Rutllant J, Fuenzalida H (1991) Synoptic aspects of the central Chile rainfall variability associated with the southern oscillation. *Int J Climatol* 11(1):63–76
- Schmidt DF, Grise KM (2017) The response of local precipitation and sea level pressure to Hadley cell expansion. *Geophys Res Lett* 44(20):10–573
- Schneider U, Becker A, Finger P, Meyer-Christoffer A, Ziese M (2018) GPCC full data monthly product version 2018 at 0.5°: Monthly land-surface precipitation from rain-gauges built on GTS-based and historical data. GPCC Full Data Monthly Product Version 7. [https://doi.org/10.5676/DWD\\_GPCC/FD\\_M\\_V2018\\_050](https://doi.org/10.5676/DWD_GPCC/FD_M_V2018_050)
- Seager R, Naik N, Vecchi GA (2010) Thermodynamic and dynamic mechanisms for large-scale changes in the hydrological cycle in response to global warming. *J Climate* 23(17):4651–4668
- Slivinski LC, Compo GP, Whitaker JS, Sardeshmukh PD, Giese BS, McColl C, Allan R, Yin X, Vose R, Titchner H et al (2019) Towards a more reliable historical reanalysis: improvements for version 3 of the twentieth century reanalysis system. *Q J R Meteorol Soc* 145(724):2876–2908
- Smith RB, Evans JP (2007) Orographic precipitation and water vapor fractionation over the southern Andes. *J Hydrometeorol* 8(1):3–19
- Staten PW, Rutz JJ, Reichler T, Lu J (2012) Breaking down the tropospheric circulation response by forcing. *Climate Dyn* 39(9–10):2361–2375
- Staten PW, Lu J, Grise KM, Davis SM, Birner T (2018) Re-examining tropical expansion. *Nat Climate Change* 8(9):768–775
- Staten PW, Grise KM, Davis SM, Karnauskas K, Davis N (2019) Regional widening of tropical overturning: forced change, natural variability, and recent trends. *J Geophys Res Atmos* 124(12):6104–6119
- Thomason LW, Ernest N, Millán L, Rieger L, Bourassa A, Vernier JP, Manney G, Luo B, Arfeuille F, Peter T (2018) A global space-based stratospheric aerosol climatology: 1979–2016. *Earth Syst Sci Data* 10(1):469–492
- Thompson DW, Wallace JM (2000) Annular modes in the extratropical circulation. Part I: month-to-month variability. *J Climate* 13(5):1000–1016
- Thompson DW, Wallace JM, Hegerl GC (2000) Annular modes in the extratropical circulation. Part II: trends. *J Climate* 13(5):1018–1036
- Ting M, Seager R, Li C, Liu H, Henderson N (2018) Mechanism of future spring drying in the southwestern United States in CMIP5 models. *J Climate* 31(11):4265–4279
- Trenberth KE, Hurrell JW (1994) Decadal atmosphere-ocean variations in the Pacific. *Climate Dyn* 9(6):303–319
- Uppala SM, Kållberg P, Simmons A, Andrae U, Bechtold VDC, Fiorino M, Gibson J, Haseler J, Hernandez A, Kelly G et al (2005) The ERA-40 re-analysis. *Q J R Meteorol Soc* 131(612):2961–3012
- van Marle M, Kloster S, Magi B, Marlon J, Daniau A, Field R, Arneeth A, Forrest M, Hantson S, Kehrwald N et al (2017) Historic global biomass burning emissions for CMIP6 (BB4CMIP) based on merging satellite observations with proxies and fire models (1750–2015). *Geosci Model Dev* 10:3329–3357. <https://doi.org/10.5194/gmd-10-3329-2017>
- Vera CS, Díaz L (2015) Anthropogenic influence on summer precipitation trends over South America in CMIP5 models. *Int J Climatol* 35(10):3172–3177
- Viale M, Bianchi E, Cara L, Ruiz LE, Villalba R, Pitte P, Masiokas M, Rivera J, Zalazar L (2019) Contrasting climates at both sides of the Andes in Argentina and Chile. *Front Environ Sci* 7:69
- Villamayor J, Ambrizzi T, Mohino E (2018) Influence of decadal sea surface temperature variability on northern Brazil rainfall in CMIP5 simulations. *Climate Dyn* 51(1–2):563–579
- Willmott CJ, Matsuura K (2001) Terrestrial air temperature and precipitation: Monthly and annual time series (1950–1999) version 1.02. Center for Climatic Research, University of Delaware, Newark
- Zelinka MD, Myers TA, McCoy DT, Po-Chedley S, Caldwell PM, Ceppi P, Klein SA, Taylor KE (2020) Causes of higher climate sensitivity in CMIP6 models. *Geophys Res Lett* 47(1):e2019GL085782

**Publisher's Note** Springer Nature remains neutral with regard to jurisdictional claims in published maps and institutional affiliations.